Bar-Ilan University

YBCO based Microwave Kinetic Inductance Detectors

גלאי השראות קינטית מבוססי YBCO

Submitted by Ariel Roitman

Ramat-Gan, Israel

September 2022

אלול התשפ"ב

Table of Contents

Abstract

Microwave Kinetic Inductance Detector (MKID) is a type of a superconducting photon detector, whose principle of operation is based on detection of changes in the 'kinetic inductance', L_k, of the superconductor. A photon with energy higher than the energy gap, Δ, breaks a Cooper pair, and thus changes the density of pairs, n_s, and the kinetic induction.

During the last decade, MKIDs based on low-T_c superconductors (LTS) were fabricated and characterized by several groups. In contrast, high-T_c superconductors (HTS)-based MKIDs are rarely described in the literature despite several intrinsic advantages associated with the use of these materials. In particular, the use of HTS is appealing in terms of applications as they need simpler and cheaper cooling systems. Moreover, the high T_c enables a relatively high working temperature and yet a small, reduced T/T_c. As the noise in the detector is influenced by the gap, being proportional to $\exp(-\Delta/k_B T)$, a reduced noise in HTS-based MKIDs is expected.

Motivated by these potential advantages of HTS-based MKIDs, I have focused in the present research work on fabrication and characterization of $YBa_2Cu_3O_{7-\delta}$ (YBCO)-based MKID. I report here on the design and fabrication of YBCO-based MKID, with a quality factor $Q_i \sim 2.5 \cdot 10^4$ and noise equivalent power, NEP $\sim 10^{-12}\ W/\sqrt{Hz}$ at 10 K, better by orders of magnitude than previously reported results. The improved performance was obtained by designing an optimal detector based on electromagnetic simulations, exploiting the SONNET software, and by calibrating a fabrication process that minimized defects and damages to the device. Extensive measurements of the temperature and field dependence of the MKID's parameters, such as the resonance frequency, f_r, and the Q-factor, yielded new information on the mechanisms controlling the changes in these parameters. In particular, zero field cooled (ZFC) and field cooled (FC) measurements of the magnetic field dependence of the resonance characteristics show substantially different behavior, indicating that both the screening currents and vortices play a role. The ZFC measurements exhibit a sharp decrease of f_r, and Q_i at low fields, up to the full penetration field (H_p), revealing the dominant role of the screening currents in this field range. In contrast, the FC measurements exhibit a

moderate decrease of f_r and Q_i with field, revealing the role of vortices and reflecting the field dependence of the penetration depth in a d-wave superconductor.

My studies pointed to several open, yet unexplored topics. A prominent example is the temperature dependence of the quasi-particle lifetime, τ_{qp}, a fundamental feature that affect the MKID performance. Contrary to theoretical predictions for divergence of τ_{qp} as $T \to 0$, measurements in LTS materials showed saturation below $\sim 0.2T_c$. To understand this behavior, I plan measuring τ_{qp} in LTS and HTS, exploiting photoexcitation and double-tunnel junction techniques. In terms of applied physics, a natural extension of my project should be in multiplexing several YBCO-based resonators that are fed by one transmission line, aiming at an increase in the spatial resolution of the imaged object. Another challenge is related to detection of X-ray photons, required in the medical and security industries. In my future studies I intend tackle those issues and challenges.

1. Introduction

During the last decades, a large variety of superconductors-based photodetectors have been developed. Examples are the Transition Edge Sensor (TES) [1], Superconducting Nanowire Single Photon Detector (SNSPD) [2], and Superconducting Tunnel Junction (STJ) [3], all benefit from the low working temperature of superconductors in reducing the Johnson Nyquist noise and the noise associated with generation-recombination of quasiparticles (qp). These detectors, which are among the most sensitive photodetectors available, suffer from a major disadvantage, namely the difficult and complex process in combining single detectors into a large array of detectors ('multiplexing') needed for imaging. The Microwave Kinetic Inductance Detector (MKID) [4], which I focus on in this dissertation, is another low temperature superconductors-based photon detector, exhibiting high sensitivity to low power flux of photons which, in contrast to other photodetectors, can be integrated into large arrays with a simple reading system ('multiplexing').

In this thesis I will describe the design, fabrication, and characterization of MKIDs, fabricated from $YBa_2Cu_3O_{7-\delta}$ (YBCO), a high temperature superconductor (HTS) material. This MKID is of interest because the HTS-based detector requires simpler and cheaper cooling systems. More important, because of the ability to work at relatively high temperature (and yet low T/T_c), the detector exhibits a lower noise [5] compared to low-temperature superconductors in the same working temperature, yielding higher sensitivity for low flux of photons. I describe in detail the process of the fabrication of YBCO-based MKIDs and characterize their intrinsic quality factor and noise equivalent power (NEP). I find at 10 K a $Q_i{\sim}2.5 \cdot 10^4$ and a NEP of $\sim 10^{-12}\ W/\sqrt{Hz}$, orders of magnitude better than previously reported [6–9] for similar MKIDs. These improved results are associated with a careful calibration of a fabrication process that avoided defects and damages to the detector.

An important part of this dissertation deals with the effect of temperature and magnetic field on the YBCO resonator. In particular, our zero-field-cooled (ZFC) and field-cooled (FC) measurements of the magnetic field dependence of the resonance characteristics, show substantially different behavior, indicating that both the screening currents and vortices play a role. The ZFC measurements exhibit a sharp decrease of the resonance frequency, f_r, and Q_i at low fields, up to the full penetration field, revealing the dominant role of the screening currents. In contrast, the FC measurements exhibit a moderate decrease of f_r and Q_i with field, revealing the role of vortices and reflecting the field dependence of the penetration depth in a d-wave superconductor.

2. Background

2.1 Microwave Kinetic Inductance Detector (MKID)

MKID is a photon detector made of superconducting microwire, whose principle of operation is based on measuring the resonance frequency in an RLC resonator [4,10,11]. The resistance in the resonator originates from the surface resistance and the inductance is the imaginary part of the surface impedance, which includes the 'kinetic inductance', L_k. (Both concepts, surface impedance and kinetic inductance, are discussed extensively in the following Sections). The kinetic inductance is inversely proportional to the density, n_s, of the Cooper pairs and, therefore, it changes as a result of photons hitting the superconductor and break pairs. To change the kinetic inductance, the photon energy $E = hf$, should be larger than the energy gap of the Cooper pairs (Δ):

$$(1)\ hf > 2\Delta(0)$$

where h is Planck constant and f is the photon's frequency.

There are many types of resonators that can be implemented in MKID. In this work I chose a half-wavelength resonator, as presented in Fig. 1a, , which has resonance frequency of:

$$(2)\ f_{res} = \frac{1}{2l\sqrt{LC}}$$

where $L = L_m + L_k$ (L is the total inductance per unit length, L_m is the geometric inductance and L_k is the kinetic inductance) and C is the total capacitance per unit length. In Figure 1 I present a picture of MKID, the equivalent RLC circuit for the resonator and typical resonance curve of MKID. Obviously, any change in n_s results in a change in the kinetic inductance and, consequently, in the resonance frequency in the RLC circuit.

By passing, we note that there are techniques to enhance quasiparticles creation even for low energy photons, *i.e.* $hf < 2\Delta(0)$. For example, a technique was developed that absorbs the heat generated by a fluence of photons, using a membrane that coupled to the device; the change in the device temperature changes the Cooper pairs density [12,13]. Another approach uses relatively high working temperatures where the device is much more sensitive to temperature changes [14].

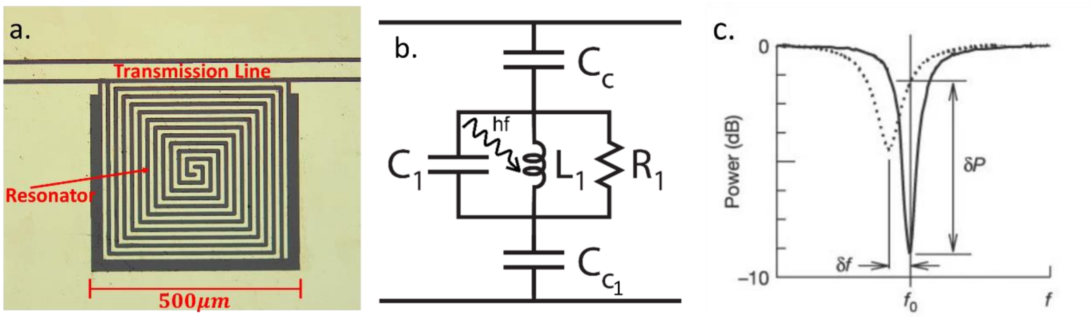

Figure 1: (a) Fabricated YBCO based MKID. Color coding: Grey: bare substrate, Green: superconductor. A half-wavelength spiral resonator was chosen because its functioning as antenna to THz radiations, which is the radiation frequency that this MKID should detect. A wide range of RF frequencies is inserted on one side of the transmission line, and measured in the output, in the other side. The resonator is coupled to the transmission line and its length defines its resonance frequency, for which the output signal is much lower than the input signal. The power versus frequency is demonstrated schematically in figure c. (b) RLC circuit, which depict schematically a MKID. A photon hitting the MKID causes a decrease in the Cooper pairs density, resulting in a change in the kinetic inductance and, consequently, in the resonance frequency [4,10,11]. (c) Solid lines: Typical resonance curve of coupled resonator MKID, at the resonance frequency, f_0, the measured power is minimum. The dashed curve represents the measured resonance frequency when a photon hits the MKID, breaking Cooper pairs and changing the resonance frequency.

2.2 Surface Impedance

The surface impedance is an important concept in treating electromagnetic (em) fields that interacts with superconductor; it allows relating the complex impedance which defines the resonator parameters, to the complex conductance, which contains the different parameters of the superconductor.

In superconductors, in the presence of AC fields the resistance and the reactance are not zero; the AC fields induces loss [15] and kinetic inductance on the surface of the superconductor. (The term 'surface' is used because fields in a superconductor penetrates only a short distance). The effects that the AC fields cause are manifested as a surface impedance of the superconductor:

$$(3)\ Z_s = R_s + iX_s$$

where X_s is the surface reactance and R_s is the surface resistance caused by mainly AC losses but also dielectric losses [16,17], impurities [18] and oxidation [19]. It was shown [20,21] that for thin films resonators, the surface impedance equals the intrinsic impedance; the later can be calculated by using known analytical/numerical models.
The relation between the impedance of the superconductor and the its complex conductivity is calculated in [22]:

$$(4)\ Z_s = \sqrt{\frac{\omega\mu_0}{\sigma_2}}\left(\frac{\sigma_1}{2\sigma_2} + i\right)$$

where ω is the angular resonance frequency, and σ_1 and σ_2 are the real and imaginary parts of the complex impedance.

From equations (3) and (4) we identify:

$$(5)\ R_s = \sqrt{\frac{\omega\mu_0}{\sigma_2}}\frac{\sigma_1}{2\sigma_2}$$

$$(6)\ X_s = \sqrt{\frac{\omega\mu}{\sigma_2}}$$

which describe the surface resistance and reactance as a function of conductivity. These parameters allow predicting the properties of a microwave resonator using, for example, the two fluid model complex conductivity that is discussed in the next section.

2.3 Kinetic Inductance

In this section I present the concept of kinetic inductance, which is one of the main sources to the reactance part in the surface impedance of superconductors in AC fields.

Kinetic inductance is a manifestation of the inertial mass of mobile charge carriers in alternating electric fields [23]. A change in the electromagnetic force (emf) will be opposed by the inertia of the charge carriers, similar to how a change in the emf is opposed by the finite rate of change of magnetic flux in an inductor. The resulting phase lag in a conductor exposed to alternating field/current is referred to as 'kinetic inductance', L_k. Kinetic inductance is observed in high carrier mobility conductors, e.g., superconductors, and in metals at high frequencies.

To understand the essence of kinetic inductance in superconductors we start with the motion equations for the Cooper pairs and the quasiparticles ("two-fluid model"), respectively [22,24]:

$$(7)\ m_e \frac{dv_c}{dt} = -eE$$

$$(8)\ m_e \frac{dv_n}{dt} + m_e \frac{v_n}{\tau} = -eE$$

Here, v_c and v_n are the velocity of the Cooper pairs and normal electrons (quasiparticles) respectively, and τ is the average time between collisions. The additional term in the second equation describes the collision between un-paired electrons.

The current density of the Cooper pairs and normal electrons can be written as:

$$(9)\ J_c = -n_c e v_c;\ J_n = -n_n e v_n;$$

where n_c and n_n are the Cooper pairs and the normal electron density, respectively.
We assume a sinusoidal electromagnetic field:

$$(10)\ J_c = J_{c0} e^{i\omega t};\ J_n = J_{n0} e^{i\omega t};\ E = E_0 e^{i\omega t}$$

where ω is the angular resonance frequency. Plugging (9) and (10) into (7) and (8) yields:

$$(11)\ J_{n0} + J_{c0} = \left(\frac{n_n e^2 \tau}{m_e(1+\omega^2\tau^2)} - i\left(\frac{n_c e^2}{\omega m_e} + \frac{n_n \omega e^2 \tau^2}{m_e(1+\omega^2\tau^2)}\right)\right) E_0\ .$$

Defining $J_0 \equiv J_{n0} + J_{c0}$ and use of $J = \sigma E$ [25], we get:

$$(12)\ \sigma = \frac{n_n e^2 \tau}{m_e(1+\omega^2\tau^2)} - i\left(\frac{n_c e^2}{\omega m_e} + \frac{n_n \omega e^2 \tau^2}{m_e(1+\omega^2\tau^2)}\right)$$

where σ is the complex conductivity.

In superconductors, there is almost no scattering of normal electrons, i.e. τ (the average time between collisions) is large so that $\omega\tau \gg 1$. Moreover, $e \to 2e$, $m_e \to 2m_e$, and not too close to T_c, $n_c \gg n_n$, so we get:

$$(13)\ \sigma \approx -i\frac{2n_c(e)^2}{m_e\omega}$$

Plugging (13) back to $J = \sigma E$, yields:

$$(14)\ E = \frac{i m_e \omega}{2n_c e^2} J$$

Using $V = \int E dl$ and (14):

$$(15)\ V = \int \frac{i m_e \omega}{2n_c e^2} J\, dl$$

For a superconducting wire with a length l, and a cross-section area A, $J = \frac{I(t)}{A}$, and assuming a uniform distribution of Cooper pairs, n_c, (15) becomes:

$$(16)\ V = i\omega \frac{m_e}{2n_c e^2}\frac{l}{A} I(t)$$

Next, we use the voltage-inductance relation, $V = L\frac{dI}{dt}$ and using an AC current $I(t) = I_0 e^{i\omega t}$

$$(17)\ V = i\omega L I(t)$$

The kinetic inductance, L_k can be identified by comparing this result with (16):

$$(18)\ L_k = \frac{m_e}{2n_c e^2}\frac{l}{A}$$

It may be more meaningful to describe the kinetic inductance with the London penetration depth, $\lambda_L = \sqrt{\frac{m_e}{\mu_0 n_c e^2}}$:

$$(19)\ L_k = \mu_0 \lambda_L^2 \frac{l}{2A}.$$

(As discussed later in this thesis, some correction factors have to be added for bulk superconductors, for thin films and for certain geometries). Equation (19) implies that the kinetic inductance depends on the dimensions of the superconductor: to obtain a large L_k one would need a long superconductor with a small cross-section. And, as discussed above, changes in n_s will result in a change in the kinetic inductance.

Referring to Equation (19), we note that the kinetic inductance depends on the London penetration depth, λ_L. Thus, the temperature and field dependence of λ_L can be measured by characterizing L_k at different temperature and fields. For example, in numerous low-T_c materials it was found empirically that [26]:

$$(20)\ \lambda_L(T) = \lambda_L(0)\left(1 - \left(\frac{T}{T_c}\right)^{\gamma}\right)^{-0.5}$$

where $\lambda_L(0)$ is the London penetration depth at T=0, and γ is a material dependent parameter. In most low-T_c materials $\gamma = 4$ [26], consistent with predictions for superconductors with s-wave symmetry (spherically symmetric wave function) of the wave function. Conflicting results ($\gamma = 1.5 - 4$) were found in high temperature superconductors (HTS) [27–29]. Our measurements, described in the Results Section, yield $\gamma = 2.6$, in the range of the expected results.

In d-wave (asymmetric wave function) superconductors, a strong linear field dependence is expected for $\lambda(H,0)$ [30]:

$$(21)\ \frac{\lambda(\mathrm{H,T})}{\lambda(0,T)} = 1 + \beta_2(T)\left[\frac{H}{H_0}\right],$$

where $H_0 = \frac{\phi_0}{\pi^2 \lambda \xi}$, ξ is the coherence length, $\phi_0 = 2.068 * 10^{-15}\,T\,m^2$ and β_2 is a factor that depends on the material. This is in contrast with the quadratic field dependence predicted for s-wave superconductors, namely [30,31]:

$$(22)\ \frac{\lambda(\mathrm{H,T})}{\lambda(0,T)} = 1 + \beta_1(T)\left[\frac{H}{H_0}\right]^2.$$

As we show in the Results Section, our results for the YBCO-based MKID adhere to the behavior expected for d-wave superconductors.

As described above, L_k depends on temperature and magnetic field, but Zmuidzinas *et al* [21] indicated that L_k depends also on the DC current which flow inside the superconductor, through the following relation:

$$(23)\ L_k(I) = L_k(0)(1 + \frac{I^2}{I_2^2} + \cdots)$$

where $L_k(0)$ is the kinetic inductance without DC current, I is the DC current, and I_2 is a constant. Intuitively, when a DC transport current is flowing inside a superconductor that exposed to high frequency alternating fields, the kinetic inductance will be higher compared to superconductor without DC current, because the transport current increases the kinetic energy of the charged particles. In the Discussion Section we exploits this concept to explain the difference between Zero Field Cooled (ZFC) and Field Cooled (FC) measurements.

2.4 Quality (Q)-Factor

In this section I describe the Q-factor and its relation to the surface impedance and the complex conductivity described in the previous sections.

The Q-factor describes how much a resonance circuit is underdamped. High Q-factors indicate that the circuit is less oppose to changes in the external electric field [32]. Commonly used Q factors in the MKID literature are denoted as Q_L, and Q_i. Q_L is the Q-factor of the whole measurement system including the MKID and Q_i is the Q-factor for the resonator. The Q_i is the interesting parameter for us because the photon interact only with the resonator.

In the context of resonators, there are two common definitions for Q_L, which are equivalent for high Q-factor resonator as describe in this thesis and used intermittently. One of these definitions is the frequency-to-bandwidth ('FB') ratio of the resonator:

$$(24)\ Q_L = \frac{f_r}{\Delta f}$$

where f_r is the resonant frequency and Δf is the resonance width at half power. The FB ratio is very useful because, as demonstrated in Fig. 1c, the measurement data is described as power versus frequency. From Eq. (24) one can see that as the Q factor increases for the same resonance frequency, the bandwidth decreases, allowing multiplexing with a larger MKID array on the same transmission line.

The other common definition for Q is the stored energy definition of the resonator:

$$(25)\ Q_L = 2\pi * \frac{energy\ stored}{power\ loss}$$

which is a very useful concept for the development process and calculation of the Q-factor as a function of superconducting parameters. As shown in ref. [32], Eq. 25 is equivalent to Eq. 24.

The Q_i for an RLC circuit, based on the stored energy definition, is defined as [4,10,11,32]:

$$(26)\ Q_i = \frac{X_s}{\alpha R_s}$$

where $\alpha = \frac{L_k}{L_m + L_k}$ is called the kinetic inductance fraction and X_s and R_s are surface reactance and resistance, respectively. Plugging Eqs. (5) and (6) into (26) yields:

$$(27)\ Q_i = \frac{2}{\alpha} \frac{\sigma_2}{\sigma_1}$$

The expressions for $\sigma_1$and σ_2 depend on the model. For example, one can use the two fluids model to calculate the quality factor, using Eq. (12), were σ_1 and σ_2 are the real and imaginary parts of σ.

In the Measurements Section, we will introduce an equation for Q_i which is based on Eq. (24) and equivalent to Eq. (27):

$$(28)\ Q_i = \frac{Q_L}{10^{\frac{S_{21}(\omega_0)_{db}}{20}}}$$

where $S_{21}(\omega_0)_{db}$ is a parameter that refers to the power (in dB) at the resonance frequency, as we elaborate on in the Measurements Section.

2.5 Noise Equivalent Power (NEP)

NEP is a measure of the sensitivity of a photodetector and it is also used as the common characteristic which describes the MKID sensitivity [11]. It is defined as the signal power that gives signal to noise ratio (SNR) of one in one hertz output bandwidth. The NEP units are, therefore, $\frac{W}{\sqrt{Hz}}$. Note that an output bandwidth of one hertz is equivalent to half a second of integration time.

The dominant noise in kinetic inductance detectors is due to random generation and recombination (g-r) of Cooper pairs inside the superconductor which causes fluctuations in the kinetic inductance. This noise results in a theoretical sensitivity limit of the detector, which is expressed as [5]:

$$(29)\ NEP_{g-r} = 2\Delta\sqrt{\frac{N_{qp}}{\tau_{qp}}}$$

where Δ is the superconductor gap energy, N_{qp} is the equilibrium number of qp in the resonator and τ_{qp} is the quasiparticle lifetime. N_{qp} and τ_{qp} depend exponentially on the temperature, yielding [5]:

$$(30)\ NEP_{g-r} \sim \exp\left(-\frac{\Delta}{K_B T}\right),$$

revealing a potential benefit from the use of HTS-based MKIDs in reducing the g-r noise due to the large energy gap characterizing HTS.

3. Research Front

MKIDs are commonly based on conventional, low T_c superconductors (LTS) such as Al T_c=1.2K [4], Hf T_c=0.4K [33], Ta T_c=4.4K [34], TiN T_c=0.4-3.5K [35], and Nb T_c=9.7K [36], which require complicated and expensive cooling systems. Apparently, high-temperature superconductors (HTS) are more attractive as they offer higher T_c and

Δ, and thus higher working temperature and lower noise, although they are suitable only in the range of ~7 THz and above. (As for breaking a Cooper pair the photon's energy should be larger than twice the gap, *i.e.* $hf > 2\Delta(0) = 3.5k_B T_c$, with T_c = 84 K for our YBCO, one obtains $f > 6.5\ THz$). Nevertheless, only a limited number of publications have addressed HTS-based MKIDs [6–9]. These works report on relatively low quality factor, Q_i ~ 4000 and relatively high Noise Equivalent Power (NEP) of ~$10^{-9}\ W/\sqrt{Hz}$ at 13 K [9,37]. This limited performance has been ascribed to damages caused to the material during the fabrication process. As we show in the Results Section, we were able to calibrate a fabrication process which minimizes damages and allows fabrication of YBCO-based MKIDs with improved performance.

In the field of microwave resonators, plenty of experimental works have been reported on the temperature and magnetic field dependence of the resonance frequency and quality factor in a wide range of temperatures and fields. In all these experiments, the results were interpreted as originating from vortices, which decrease the density of Copper pairs in their core, and increase the losses during their movement [38–41]. Our magnetic characterization of the YBCO-based MKID confirm indeed the role of vortices, but only in field-cooled measurements. In contrast, a dominant role of the screening currents was revealed in zero-field-cooled measurements.

4. Research achievements

I summarize below the main achievements of this research project. Part of these results are summarized in a paper submitted for publication, entitled "*Characterization of $YBa_2Cu_3O_{7-\delta}$ coplanar resonator for Microwave Kinetic Inductance Detectors*".

- Designing and fabricating YBCO-based MKID with Q_i~$2.5 \cdot 10^4$ and noise equivalent power, NEP $\sim 10^{-12}\ W/\sqrt{Hz}$ at 10 K, better by orders of magnitude than previously reported results [9].
- Characterizing the effect of temperature and magnetic field on the performance of YBCO MKID, finding a degradation in Q_i as the magnetic field/temperatures increase and a non-linear behavior in low magnetic fields.

- Revealing the dominant role of the screening currents in comparison with the role of vortices. This is found in zero-field-cooled measurements. In contrast, field-cooled measurements reveal the role of vortices.
- Demonstrating the use of the YBCO-based MKID in measurements of basic physical parameters, such as the London penetration depth below T_c and as function of magnetic field.

The rest of this dissertation is organized as follows. In Section 5 I discuss the research methods, including the choice of material for the MKID, MKID geometry and its design parameters, fabrication methods and the advantages and disadvantages of each method. The experimental setup is also described with its cooling system, the insert which holds the detector, and the measurements setup.

Section 6 present our simulations and experimental results of two different measurements protocols, which allowed us to reveal the effect of screening currents on the kinetic inductance.

Finally, in section 7 I discuss the preferred method to calculate the kinetic inductance fraction and conclude by deriving the magnetic field and temperature dependence of the London penetration. In addition, I explore the effect that vortices and screening currents on the kinetic inductance.

5. Research Methods

5.1 Materials

For the MKID material I chose Yttrium Barium Copper Oxide (YBCO) which is part of the crystalline chemical compounds that displays high temperature superconductivity. This choice has been motivated in part by our experience with fabricating YBCO nanostructures [42] and, of course, YBCO may be appealing for applications because of the potential significant saving in cooling costs. Also, specifically for MKID, using YBCO is expected to present lower g-r noise in comparison with state-of-the-art LTS based MKIDs. YBCO thin films of thickness d = 50 nm, with a layer of 50 nm gold on top, were grown on MgO substrate (The MgO substrate was chosen because it has low losses and because of its high permittivity which allows more compact resonator geometry). The films were grown by Ceraco

Ceramic Coating LTD [43] , which noted that films that are thinner than 50 nm presented a low transition temperature. In Figure 2 we describe the temperature dependence of the resistance of the 50 nm Ceraco YBCO film, showing T_c = 84 K. We chose the thin (50 nm) YBCO films to benefit from the resulted high kinetic inductance. We note that these films are stable and resilient to fabrication processes. The 50 nm gold layer ensures protection of the YBCO and allows low resistance contact points. The MgO substrate was chosen because it has low losses and because of its high permittivity which allows more compact resonator geometry.

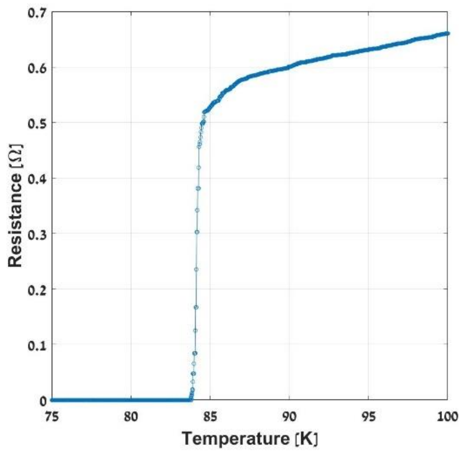

Figure 2: Resistance *vs.* temperature of 50 nm YBCO film with 50 nm gold on top. The low resistance above the phase transition is due to the gold layer.

5.2 MKID geometry

5.2.1 CoPlanar Waveguide (CPW)

CPW is a type of a planar transmission line and it is used to convey signals at microwave frequencies [44]. CPW consists of a signal conducting track on dielectric substrate, together with a pair of ground conductors, on the two sides of the track, as presented in Figure 3. The conductors, as the name 'CoPlanar' implies, are on the same side of the substate which simplify the fabrication process significantly and thus it is the most common transmission type for MKIDs. The MKID in this work is also based on CPW transmission line.

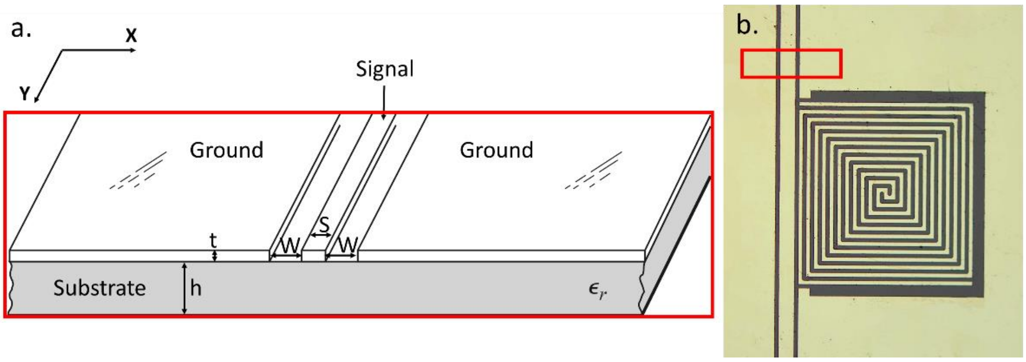

Figure 3. (a) A cross-section of MKID's CPW transmission line. (b) The resonator and the transmission line. The red rectangle marks the area that is described in details in (a) [32]. S is the width of the signal track and W is the gap width between the signal track and the ground planes, h is the substrate thickness and t is the film thickness. The wave propagates in Y direction.

The effective dielectric constant for a CPW is $\epsilon_{eff} = \frac{1+\epsilon_{r_{substrate}}}{2}$ [45], which is approximately half of the dielectric constant of the substrate, because the electric and magnetic field propagate both in air and in the substrate. The geometric inductance for CPW geometry per unit length is given by [46]:

$$(31)\ L_m = \frac{\mu_0}{4}\frac{K\left(\sqrt{1-k_0^2}\right)}{K(k_0)}$$

where K is a complete elliptic integral from the first kind, μ_0 is the vacuum permeability, and $k_0 = \frac{S}{S+2w}$, where S and w are defined in Figure 3. The kinetic inductance for CPW is similar that described in Eq. (19), but there is a geometrical factor that needs to be added, so L_k per unit length is [46]:

$$(32)\ L_k = \mu_0 \frac{\lambda_L^2}{dw} g$$

where d is the film thickness and

$$(33)\ g = \frac{1}{2k_0^2 K(k_0)}\{-\ln\left(\frac{d}{4w}\right) - \frac{w}{w+2s}\ln\left(\frac{d}{4(w+2s)}\right) + \frac{2(w+s)}{w+2s}\ln\left(\frac{s}{w+s}\right).$$

The impedance of a CPW depends on the inductance and needs to match 50 Ω, *i.e.* to the coaxial cables impedance. The following definition of the CPW impedance [47]

$$(34)\ Z_0 = 30\frac{\pi}{\sqrt{\left(\frac{\epsilon_r+1}{2}\right)}}\frac{K\left(\sqrt{1-k_0^2}\right)}{K(k_0)}$$

allows us to match the MKID transmission line impedance to $50\,\Omega$. The resonator impedance itself does not have to be $50\,\Omega$ because it is coupled to the transmission line.

Because the detector is based on detection of changes in the kinetic inductance, we have to assure that the kinetic inductance will be as high as possible compared to the total inductance; this may be achieved by decreasing the cross section area of the spiral resonator. It is convenient to use the kinetic inductance fraction, defined above in sub-section 2.4:

$$(35)\ \alpha = \frac{L_k}{L_k + L_m}$$

to indicate the ratio between the kinetic inductance and the total inductance.

5.2.2 Resonator geometry

I adopted a design described in Ref. [36] consisting of CPW transmission line to which we capacitively couple a halfwave length spiral resonator, as presented in Fig. 4. This design was chosen with a future project in mind. Specifically, the design is similar to a THz antenna [48] operating at ~100 GHz and above [49]. This design can be used as photon absorber in a future projects involved detection of sub-THz photons, such as passive-THz imaging systems, which need a very sensitive THz detector [14].

As described at section 5.1, the superconductor layer thickness is 50 nm, to maximize the kinetic inductance. The transmission line dimensions, as described in figure 3, are: $S = 40\ \mu m$ and $w = 10\ \mu m$, yields to $Z_0 = 43\ \Omega$ using Eq. (34), which is lower than the $50\ \Omega$ needed, but we note that the calculations are based on mathematical formulas, ignoring real life effects such as finite ground planes, finite dielectric thickness, *etc.*. Indeed, the impedance, using EM simulations which discussed extensively in section 6, for the mentioned dimensions is $46\ \Omega$. Clearly, we should consider changing the next version MKID transmission line gap to yield exactly 50 Ω.

The spiral resonator line width and the space between lines are $10\ \mu m$. The total length is $11{,}000\ \mu m$ which approximately equal to half-wavelength. I used those parameters to calculate L_k and L_m yielding kinetic inductance fraction of $0.73\ (\alpha_{calc})$, a value implying that the kinetic inductance is the dominant part of the total inductance. We note that the resonator does not have a classical CPW geometry, so the L_m may be inaccurate in this case (this point will be further discussed in Section 7).

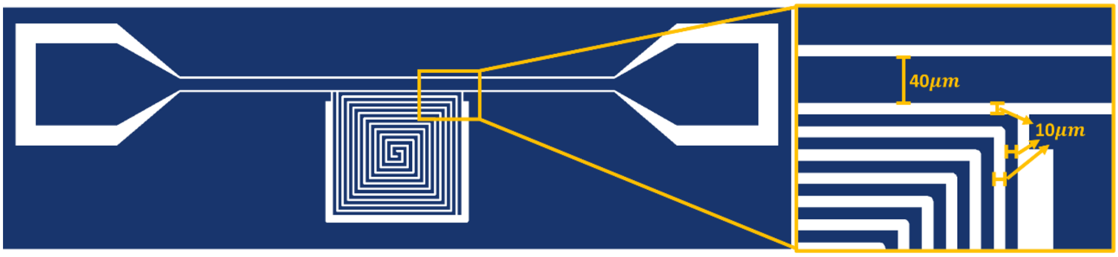

Figure 4: Schematic description of the YBCO MKID. Dark and white regions are the YBCO film and the bare MgO substrate, respectively. The pads at the end of the transmission line are used for wire bonding.

5.3 Fabrication process

YBCO thin film is sensitive and easily damaged when expose to solvents and plasma. Moreover, YBCO may be damaged when it is heated to temperatures above 100 C, temperatures that are common in usual fabrication process. Therefore, its fabrication processes exhibit great challenges. In the following section we present two fabrication processes, one is based on e-beam lithography and the other is based on Maskless Laser Aligner (MLA) lithography. In both methods, the gold layer, which protects the YBCO, was removed from the resonator only at the end of the fabrication process in order to maintain the films protection as long as possible throughout its fabrication.

5.3.1 Resist Coating 1

The resist coating for both processes was made using resist spinner.

<u>E-beam: </u>The sample coated with PMMA A6 resist at 4000 rpm speed, and afterwards a baking on hot plate for 3 minutes at 100 C – The specifications of the resist require 1 minute at 180 C, but 180 C will damage the YBCO, as presented in Figure 5 were the critical temperature is less than 50 K, which is a major decrease compare to figure 2, were the critical temperature was 84 K.

<u>MLA:</u> The sample coated with AZ1518 resist at 4000 rpm speed, and afterward a baking on hot plate for 1 minutes at 100 C.

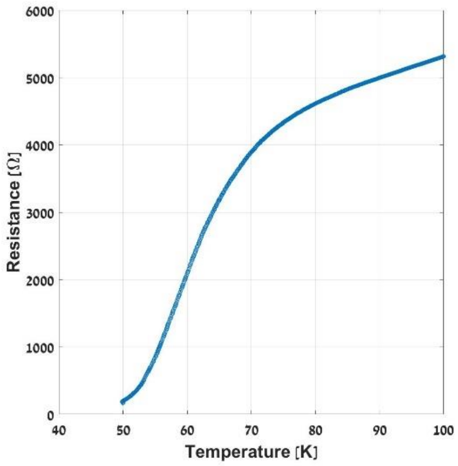

Figure 5: Resistance versus temperature for an YBCO wire without gold. The wire was baked on hot plate at 180 C for 60 seconds. Note the absence of the 84 K transition observed in the non-fabricated YBCO film (Figure 2).

5.3.2 Lithography 1

In this stage of lithography, we wrote the transmission line, resonator and pads as presented in Figure 4.

<u>E-beam:</u> We used the Crestec electron-beam CABL-AP series (e-beam), which has a very long writing times due to its high writing resolution (a few dozens of nm) which is not required for the MKID. A voltage of 50 kV with current of 1 nA was applied, and the exposure time was 0.5 μs. After the lithography the sample inserted into diluted 1:3 AZ351b: isopropanol developer for 2 minutes and then in $H_2 0$ to stop the development process.

<u>MLA:</u> We used the Heidelberg Instruments maskless aligner (MLA150), which offers short writing times and the resolution that we need. A 405 nm wavelength laser with dose 115 $[mJ/cm^2]$ beam was used. After the lithography the sample was inserted into diluted 1:4 AZ351b: $H_2 0$ developer for 1 minute and then in $H_2 0$ to stop the development process.

5.3.3 Ion Milling

This is the most destructive stage in the fabrication process, and that was the stage that motivated us to test both fabrication methods. It became clear to us that if the milling process was not calibrated precisely, the photoresist of the MLA could burn, and require solvents to remove it, a process that damages the YBCO. Unfortunately, a reactive ion etching (RIE) was not possible because the gold layer is not reactive. A wet etch is not possible well since as we could not find a solvent that did not damage the YBCO.

We used Bestek's milling sputter system for the Ar-milling process, which is identical for MLA and e-beam lithography methods. To avoid overheating the sample and destroying the resist, a thermal grease was implemented between the sample and its holder. Then, instead of working with one long pulse, we employed 6 pulses of 5 seconds to remove the excess YBCO and gold, and between each pulse we cooled down the sample with flow of nitrogen gas on the sample inside the machine. We highly recommend working with shorter pulses because, from our experience, the milling process is not stable, and sometimes (although not always) burns the photoresist.

5.3.4 Resist removal 1

As long as the milling process is precisely calibrated, acetone will remove MLA's resist and e-beam's resist from the sample. Sometimes a few seconds of sonication will be required, but this process does not damage the YBCO. Problems start when the milling process is not calibrated precisely. The e-beam resist is much more resilient and always was removed by using acetone. The photoresist was much more sensitive to heating and milling and stuck to the sample. To remove such photoresist, a much stronger processes are needed. We found that when the YBCO is soaked in Acetone solvent, $T_c = 84\ K$ is maintained, see the R(T) curve for this sample in Figure 6. In samples which were soaked in NMP, T_c was reduced to ~80 K. When the sample soaked in NMP was exposed to O_2 plasma, the critical temperature was further reduced to about 35 K. Moreover, we found that also O_2 plasma alone can remove stuck photoresist, but can also damage the YBCO.

From our experience, although the e-beam lithography writing times is much higher, the e-beam resist is more resilient in the milling process and can be removed in acetone that did not damage the YBCO.

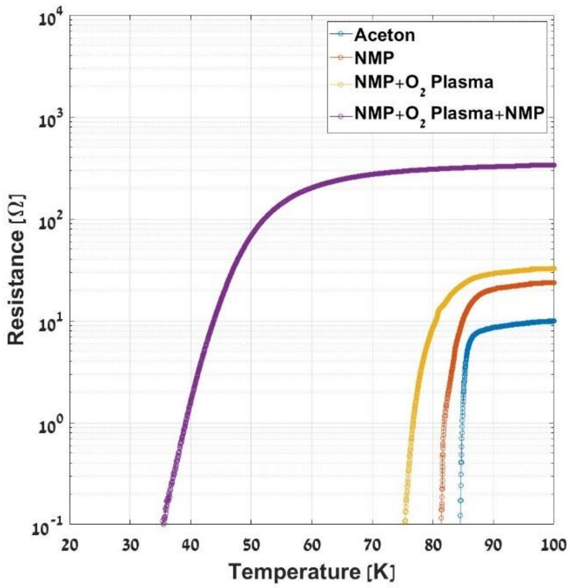

Figure 6: Temperature dependence of the resistance of four YBCO films after ion milling with different solvents.

The next lithography step was made to remove the gold layer from the resonator, so that the incident photons will interact with the YBCO and not with the gold. Of course, the gold was not removed from the pads. Moreover, because the gold removal steps do not affect the resist, the photoresist can be removed easily with acetone, so the MLA method can be used for shorter writing times.

5.3.5 Resist Coating 1

Same as 5.3.1

5.3.6 Lithography 2

In this lithography stage we wrote an area above the resonator itself, so that during gold etching stage only the gold above the resonator is removed.

Everything else is the same as in 5.3.2

5.3.7 Gold etch

To remove the gold layer above the resonator we used commercial gold etcher, which is based on potassium iodide and iodine. The sample was inserted to solvent with 1:4 ratio of gold etcher:H_2O for 1 minute to remove the excess gold and then inserted to H_2O to stop the etching process.

5.3.8 Resist Removal 2

Basically, same as 5.3.4, but because the gold etching process does not affect the resist, the photoresist is also removed easily with acetone.

In Figures 7 and 8 we plot the R(T) curves for the two fabricated MKIDs (*i.e,* the MKIDs fabricated by using e-beam lithography and MLA lithography, respectively). The resistance was measured on the transmission line. In the e-beam lithography process, after the dose calibration of the e-beam, we achieved $T_c = 84\ K$ at the first sample fabrication. We fabricated a few more samples using the e-beam process and all of them achieved the same results. The key in this process is that the e-beam resist is very resilient to the milling process. In contrast, though we achieved similar critical temperature using the MLA lithography, several of the samples did not work because the resist could not be removed without using strong solvents. We thus conclude that the use of e-beam in the first lithography stage is highly recommended.

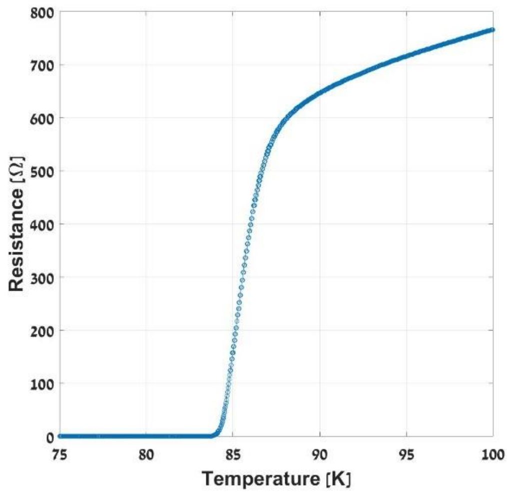

Figure 7: R(T) showing the superconducting phase transition in an MKID fabricated by using e-beam. The transition is maintained at $T_c = 84\ K$, as in a new film.

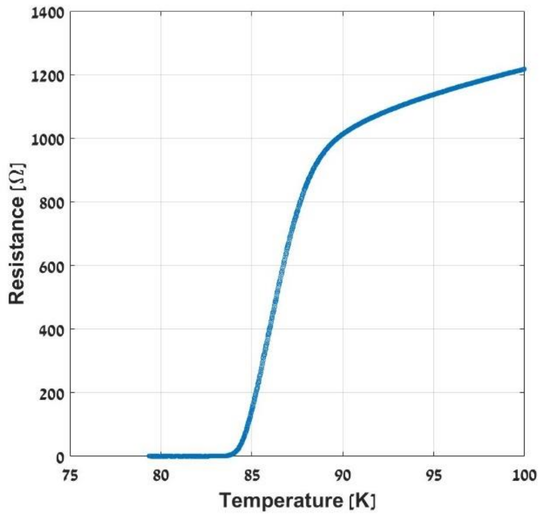

Figure 8: R(T) of fabricated MKID using MLA. $T_c = 84\ K$ as in a new film.

5.4 Cooling system

The MKID and its supplementary components were inserted inside the sample space of a commercial "Quantum Design" Physical Property Measurement System (PPMS). The PPMS is capable of cooling the sample to a minimum temperature of 2 K and to generate a DC magnetic field up to 9 Tesla. These extended ranges were used us to study the behavior of resonator as function of temperature and magnetic field.

5.5 Measurement system

The measurement system is described schematically in Figure 9. The main component in the measurement system is a Keysight P5024A Vector Network Analyzer (VNA). The VNA has a sync RF source and receiver that connect to SMA RF input/output connector. The VNA measures changes in phase and amplitude between the ports.

To calculate the intrinsic Q-factor, we used the formula (same as equation (28) [32]:

$$(36)\ Q_i = \frac{Q_L}{10^{\frac{S_{21}(\omega_0)_{db}}{20}}}$$

where $Q_L = \frac{f_{res}}{\Delta f}$ is defined in Eq. 24. $S_{21}(\omega_0)_{db}$ is a parameter that refers to the power (in dB) at the resonance frequency. As mentioned in section 2.4, Δf is the bandwidth for half power. When the resonance deep is close to 3dB or shallower Δf can't calculated as respect to half power, and need to be calculated with:

$$(37)\ S_{21} = |S_{21min}|\sqrt{\frac{2}{1+|S_{21\text{min}}|^2}}$$

The parameters above can be measured using the VNA, when its operation mode is the measurement of loss between the two ports on the MKID in linear scale (S21) as function of the resonance frequency. When $S_{21min} \gg 3dB,\ S_{21} \to \sqrt{2}$ which in logarithmic scale is 3dB.

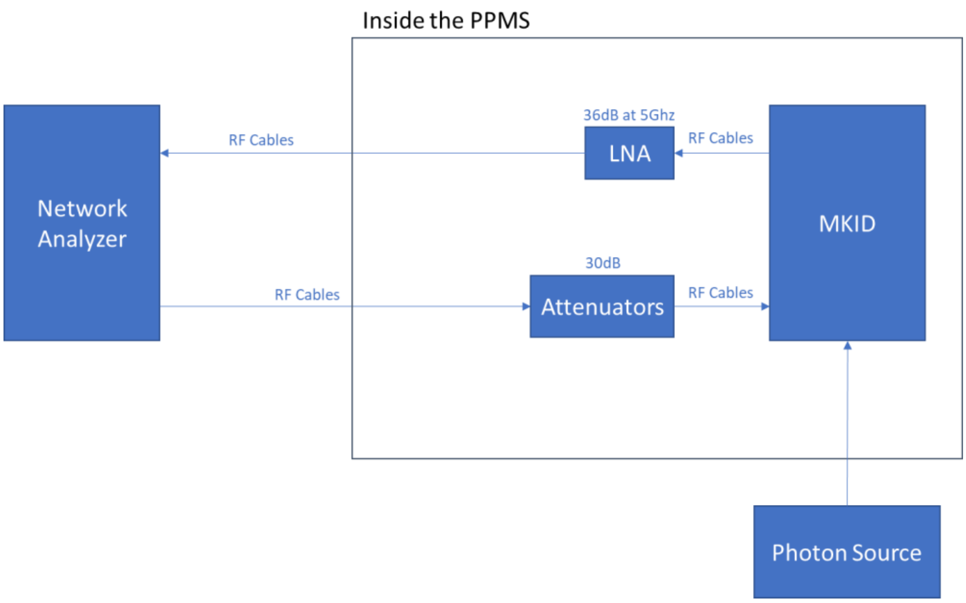

Figure 9. Measurement setup.

The purpose of the attenuators in Figure 9 is to reduce the noises power that entered to the MKID such as the thermal noise of the VNA. The LNA (Low Noise Amplifier) is based on High-Electron-Mobility-Transistor (HEMT) because semiconductor-based transistors do not work at cryogenic temperatures. The LNA is used to amplify the signal from the MKID. The LNA is mounted as close as possible to the lowest temperature level inside the PPMS to reduce its internal thermal noise. The RF cables meet cryogenics specs of low thermal conductance cables; this is necessary because one end of the cable is at room temperature, and other end is connected to the MKID at the cold stage of the system. The photons source is based on the 1064 Nd:YAG laser with an optical fiber that guided the transmitted photons to the MKID's spiral resonator.

In Video 1 we demonstrate the effect of the laser photons on the resonance frequency of YBCO based MKID. The video has taken straight from the VNA, which measure the transmission power as power of frequency. The 'deep' in the power is at the resonance frequency, which changes when a pulse of 1064nm laser hits the MKID.

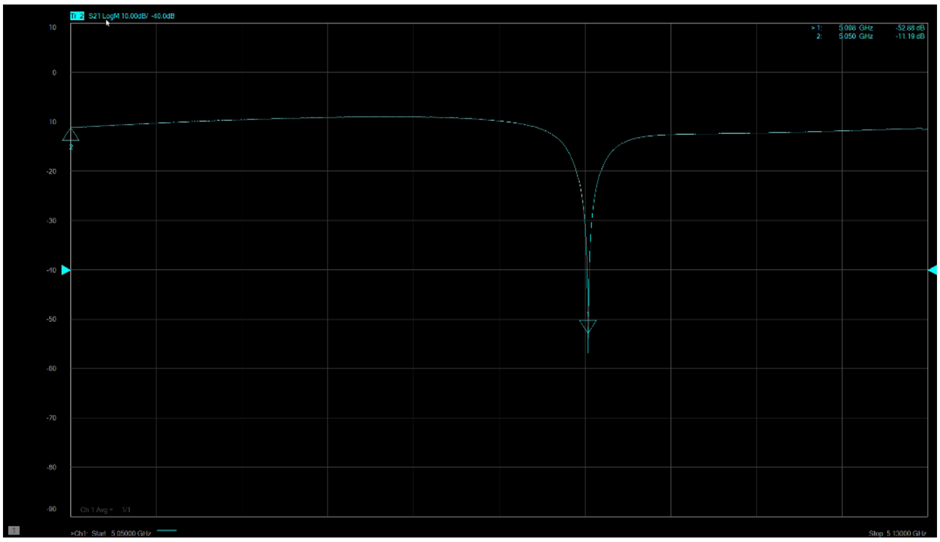

Video 1: Measurement of the power (dB) as function of frequency of YBCO based MKID. A pulse of 1064 nm laser shifts the resonance frequency.

6. Results

This section is divided into two parts: (1) results from simulations for the MKID that has been made using 'SONNET Precision Electromagnetics' simulation software. (2) Measurements made for e-beam fabricated MKID under various of temperatures and magnetic fields, including NEP estimation of the detector.

6.1 MKID Simulations

The SONNET [50] software is an electromagnetic simulation software that includes the option to simulate superconductors. One of our purposes in the simulations was to determine the resonance frequency of the MKID with and without kinetic inductance, which allow us to calculate the kinetic inductance fraction, and compare it to $\alpha_{calc} = 0.73$ as calculated from the equations in Section 5.The kinetic inductance is the heart of the device and is important for determining the temperature and magnetic field dependence on the penetration depth, as discussed in the Discussion Section. The kinetic inductance can be modeled in the simulation as a surface inductance, L_s. The surface impedance is defined as [50]:

$$(38)\ L_s = \mu_0 \lambda_L$$

where μ_0 is vacuum permeability and λ_L is London penetration depth. The superconducting model in SONNET does not include thickness/temperature options, so those parameters can be added to the model through λ_L. In our case, we can include the MKID thickness using pearl penetration length, namely the effective λ_L for a thin film with thickness $d \ll \lambda_L$. The Pearl penetration length is [26]:

$$(39)\ \lambda_{\text{eff}} = \frac{\lambda_L^2}{d}.$$

We take $\lambda_L(T = 0) = 230\ nm$ [28] for YBCO and MKID thickness of 50 nm, which results in λ_{eff} of 1058 nm and, therefore, $L_s = \mu_0 \lambda_{\text{eff}} = 1.31\ pH$. Similar calculations can be made for the temperature dependence, but I assume T<<T_c so that $\lambda_{L,T \ll T_c} = \lambda_{L,0}$ and for simplicity we ignore AC losses.

Figures 10 and 11 are simulation results, in terms of the transition loss between each side of the transmission line, as a function of frequency, of the designed MKID, without and with kinetic inductance, respectively. From Eq. (2) we can expect that the resonance frequency will decrease when considering the kinetic inductance in the simulations, as actually happens. The resonance frequency of the resonator, when ignoring the kinetic inductance, is $6.202GHz$ (see Fig. 10). This value may be compared to the resonance frequency of a normal metal (without kinetic inductance) half wavelength CPW resonator [51]:

$$(40)\ f_{res} = \frac{c}{2l}\sqrt{\frac{2}{1+\epsilon_r}}$$

where f_{res} is in GHz, c is speed of light in km/s, l is the resonator length in μm and ϵ_r is the dielectric constant of the substrate. Using Eq. (40) we find that $f_{res} = 5.8GHz$ which is less than 10% of deviation compared to the simulation; This is reasonably close.

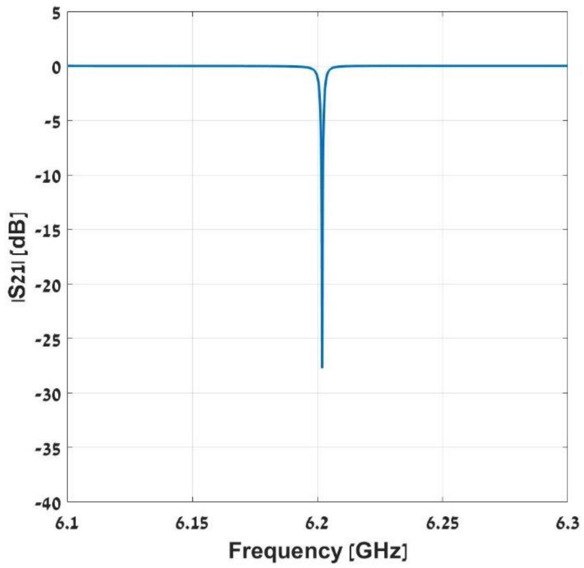

Figure 10: SONNET simulation of MKID with geometric inductance only. $f_{res} = 6.202GHz$.

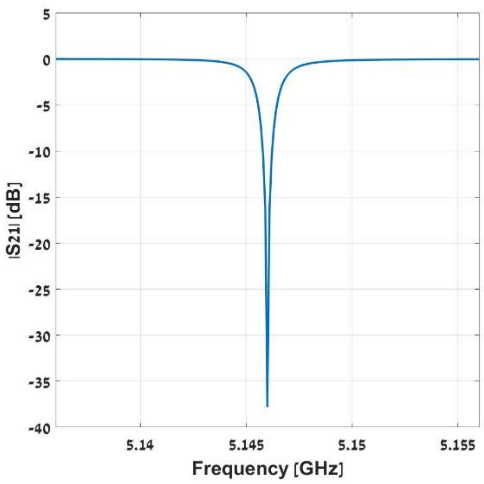

Figure 11: SONNET simulation of MKID with geometric *and* kinetic inductance. $f_{res} = 5.146\ GHz$. As expected, this value is lower than f_{res} for simulation without kinetic inductance.

6.2 MKID measurements

Figure 12 shows the resonance curves of the YBCO MKID, measured between 4 and 60 K, exhibiting a monotonic downward change of f_r and decrease of Q_i as the temperature rises. At $T \ll T_c$ we find that the measured resonance frequency is almost identical to the simulated resonance frequency. The 'deep' depth is deeper in the simulations because it is due to losses which ignored in the simulations. At 10K $Q_i = 5 \cdot 10^4$, an order of magnitude higher than that reported in Ref. [9]. In calculating the characteristics of the MKID, *i.e.*, responsivity and Noise Equivalent Power (NEP), we follow the approach of Refs. [9] and [52]. The responsivity is calculated as $R_{es} = (\Delta|S_{21}|^2)/\Delta P$, where $\Delta|S_{21}|^2$ and ΔP denote the change in the response power and incident light power, respectively. For an incident laser power of 12 μW, the power response due to a 1 second pulse was about $2\, nW$, yielding a responsivity of $0.16 \cdot 10^3 \mu W/W$. The NEP is calculated as $\frac{P_n}{R_{es}\sqrt{\Delta f}}$, where P_n is the noise power in a bandwidth of Δf. The noise power at 10 K was about -108 dBm in a bandwidth (BW) of 10 kHz, yielding NEP of about 10^{-12} $W/\sqrt{Hz}$, significantly better that the value $10^{-9} W/\sqrt{Hz}$ reported for 13 K in Ref. [9].

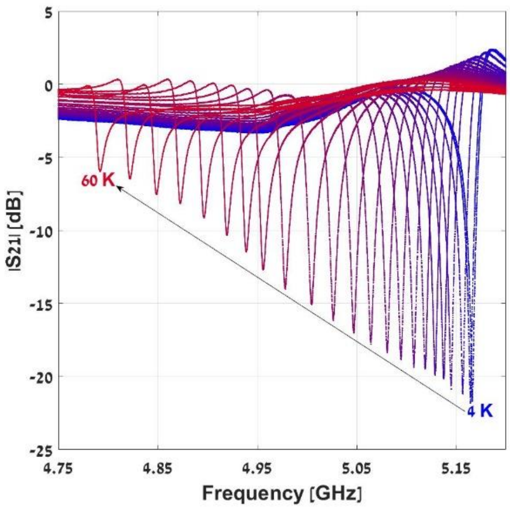

Figure 12. Resonance curves of the YBCO MKID measured in zero field at T = 4, 10, 15, 20, 22.5 to 47.5 K in steps of 2.5 K, and 49.5 to 60 K in steps of 1.5 K.

In Zero Field Cooled (ZFC) measurements, the sample is cooled in zero field from above T_c to the measurement temperature, where changes in the magnetic field are done. In this mode of measurements, the spatial dependence of the induction and screening currents are described by the Bean model [53] and its extension for perpendicular fields [54] in narrow samples.

Figures 13 and 14 describe the measured temperature dependence of f_r, and Q_i, respectively, measured in various magnetic fields up to 0.5 T after ZFC. For each field, both quantities decrease monotonously with temperature. The decrease of f_r is expected because the Cooper pairs density decreases as the temperature increases, yielding to increase in the kinetic inductance and decrease in the resonance frequency; This can be seen mathematically from Eqs. (2), (20) and (21) .The decrease in Q_i is expected from Eq.(26); the loss, R_s, increases as the temperature increases, so that Q_i should decrease.

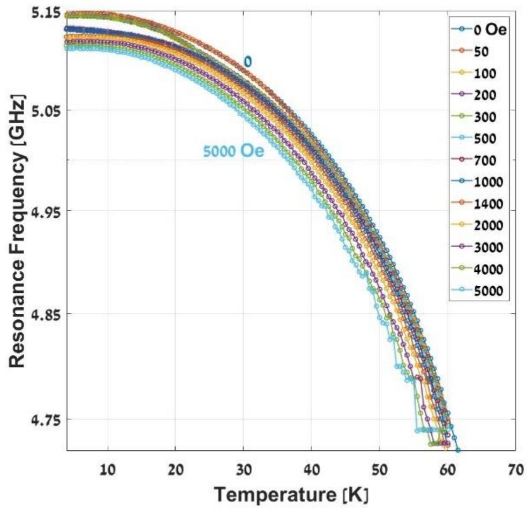

Figure 13. Temperature dependence of the resonance frequency, f_r, at the indicated fields applied after zero-field-cooling.

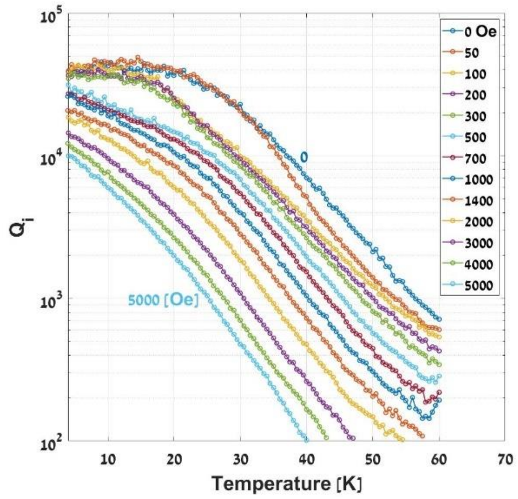

Figure 14. Temperature dependence of the internal quality factor, Q_i, at the indicated fields applied after zero-field-cooling.

Figures 15 and 16 show ZFC measurements of the field dependence of f_r and Q_i at 10 K, respectively, with fields up to 5 T , down to -5 T and back to zero. Both parameters decrease with field, in accordance with the data reported for a different YBCO resonator [55]. Note, however, the sharp drop in f_r and Q_i at low fields, as described in more details later in this section. Also, an hysteresis effect is observed at low fields only for f_r, similar (but not identical) to that previously reported for a Nb resonator [38]. (To be more specific, In Figure 15 b we mark a green square that indicates an increase in f_r when the magnetic field is decrease from 0, while in , Ref. [23], in the same field range, the resonance frequency decreases). The difference between the hysteresis reported here and that reported in [23] is not yet clear to us.

In Figures 17 and 18 we present similar results to Figures 15 and 16 but measured at different temperatures. As temperature increases, the values of f_r and Q_i decrease, a reasonable result because as temperature increases the kinetic inductance and the losses increase. Moreover, the rate of change of f_r and Q_i with the magnetic field increases as temperature increases. The main reason is that the change in the kinetic inductance and losses is not linear. As the temperature/magnetic field increases, the change in L_k and R_s is sharper.

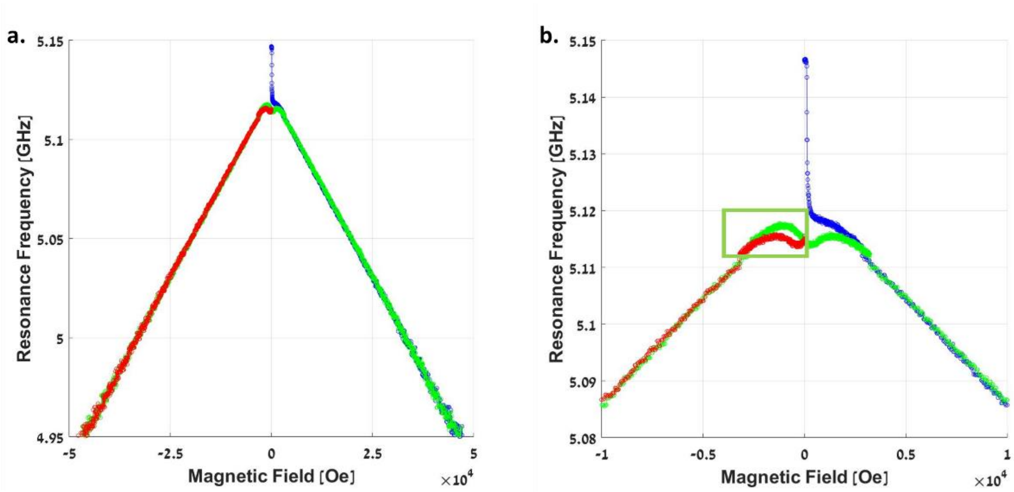

Figure 15. Resonance frequency, f_r, at 10 K as a function of magnetic field, after zero-field-cooling. In blue – sweep up from 0 to 5 T. Green – sweep from 5T to -5T. Red – sweep from -5T back to 0. The sharp decrease in the f_r is only from the virgin state. The green square points to the field range where an increase in f_r is observed when the magnetic field is decreased from 0. Figure 15 (b) zooms on the hysteresis in f_r at low fields.

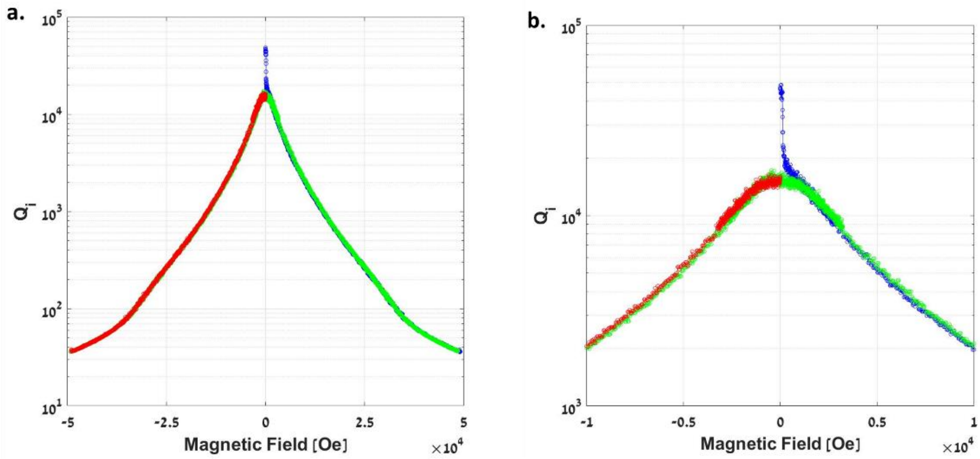

Figure 16. Internal quality factor, Q_i, at 10K as function of magnetic field, after zero-field-cooling. In blue – up sweep from 0 to 5T, in green – sweep from 5T to -5T, and in red – sweep from -5T back to 0. The sharp decrease in the Q_i is only from virgin state. (b) is zoom on Q_i at low fields.

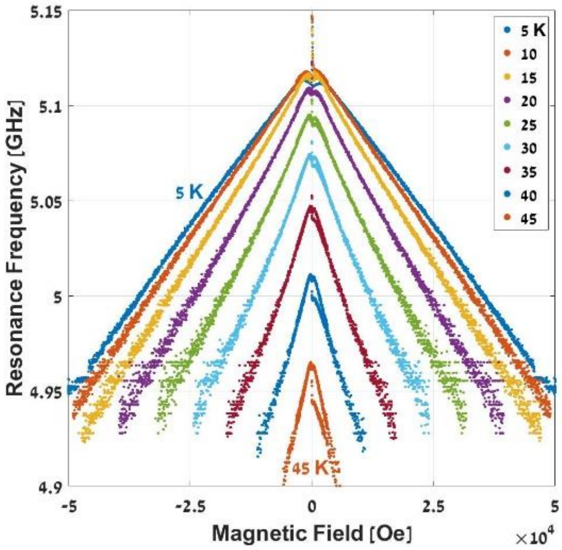

Figure 17. Resonance frequency, f_r, at different temperatures as function of magnetic field, after zero-field-cooling.

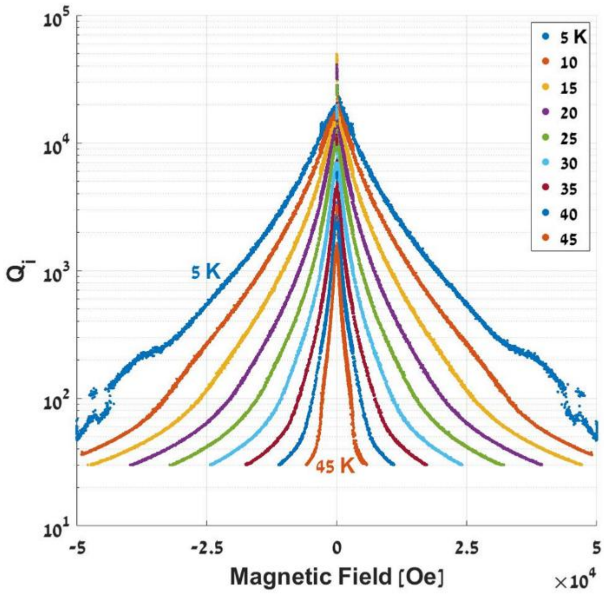

Figure 18. Internal quality factor, Q_i, at different temperatures as function of magnetic field, after zero-field-cooling.

The next measurement was made in a different method. Instead of varying the magnetic field at the superconducting phase, we change the magnetic field in the normal phase, and then cooled down the MKID. This field applying protocol, called Field Cooled (FC), is fundamentally different from ZFC protocol as there are no screening currents in the device.

As is clear from Figure 19, the field dependence of f_r shows a substantially different behavior in FC and ZFC measurements for data measured at 20 K. While the FC measurements show a moderate decrease with the field in the entire field range, the ZFC measurements exhibit a more complex behavior: Initially, f_r shows a weak field dependence, followed by a sharp drop after which f_r continues to decrease moderately in parallel to the FC data. The inset to Figure 19a zooms on the low field behavior of the ZFC and FC data. This unique behavior at low fields is exhibited in Figure 19b for various temperatures, showing that the sharp decrease of f_r is shifted towards lower fields as the temperature increases.

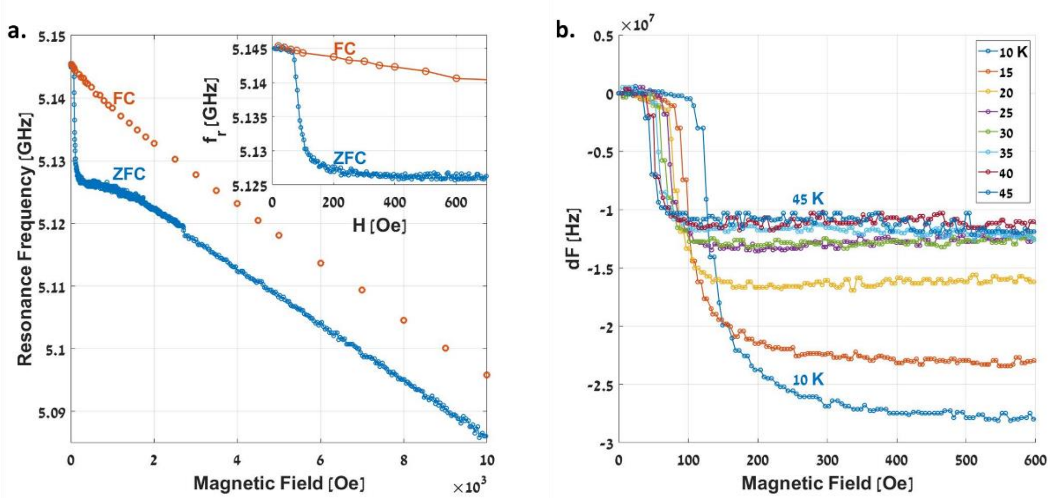

Figure 19. (a) Resonance frequency as a function of magnetic field in FC (upper curve) and ZFC measurements (lower curve) at T = 20 K. Inset: Zoom-in on the low fields data. (b) Field dependence of $df = f_r(H) - f_r(0)$ at low fields in ZFC measurements, at the indicated temperatures.

7. Discussion

The improved performance achieved in our YBCO MKID as compared to that reported previously, is presumably associated with our thin YBCO film (50 nm) and a careful control of the fabrication process. Thinner films give rise to a larger ratio of the kinetic to total (kinetic + magnetic) inductance, improving the sensitivity of the MKID. Also, employing e-beam lithography and keeping the temperature of the sample below 100 C during the entire process, help in minimizing the damage to the film, improving the quality factor and the NEP.

The kinetic inductance fraction (α) is an important parameter, indicating 'how' dominant is the kinetic inductance in the total inductance. A precise calculation of α is needed in order to be able to find accurately the parameters β_2 and γ which define the magnetic field and temperature dependence of the London penetration depth (see Eqs. (20) and (21), respectively).As mentioned in section 5.2.2, calculations based on L_m and L_k as defined in Eqs. (31) and (32), respectively, yield $\alpha_{calc} = 0.73$ for our MKID geometry. A point of concern in our calculations is that Eq. (31) is for CPW with a center strip and ground planes from both sides, whereas our resonator geometry is somewhat different (see Figure 4,) namely that the center strip is rewound and does not have ground planes around it. In an effort to estimate the error in α_{calc}, we used also the SONNET simulations as a tool in calculating α. We can use Eq. (2) and define for f'_{res} that $L = L_m$ and for f_{res} that $L = L_m + L_k$. The ratio between f'_{res} and f_{res} gives the ratio between L_m and L_k.

$$(41)\ \frac{f'_{res}}{f_{res}} = \frac{2l\sqrt{(L_m+L_k)C}}{2l\sqrt{L_m C}} = \frac{\sqrt{L_m+L_k}}{\sqrt{L_m}}$$

which yields

$$(42)\ L_m = \frac{L_k}{\left(\frac{f'_{res}}{f_{res}}\right)^2 - 1}$$

For f'_{res} which includes only the magnetic inductance, we can use the value from the SONNET simulation in Figure 10, $f'_{res} = 6.202\ GHz$. For f_{res}, which includes both magnetic and kinetic inductance, we can take value from SONNET simulation in Figure 11, of the measured value, which is almost identical to the simulate one, $f_{res} = 5.146 GHz$. Using (38), f'_{res} and f_{res}, yields $L_m = 2.2 L_k$, which gives $\alpha_{sim} = 0.31$, significantly different from α_{calc}. In both calculations, it is obvious that we cannot ignore L_m in our calculations. To examine which calculation method for α is more accurate, we use Eq. (2), together with London penetration depth temperature dependence (Eq. 20) and the definition of L_k to get:

$$(43)\ f_{res} \sim \frac{1}{\sqrt{L_k\left(1-\left(\frac{T}{T_c}\right)^{\gamma}\right)^{-0.5} + L_m}}$$

In figure 20 we use the MATLAB curve fitting function, to find the best fit of Eq. (20) to the measurement of $f_{res}(H = 0)$ as a function of temperature for both options of α, when γ is a parameter that the MATLAB will find for each α. When using α as calculated from the simulations, ($\alpha_{sim} = 0.31$), the fit is reasonably good with γ value of 2.6 that is known in the literature for d-wave superconductors, in contrary to the fit using $\alpha_{calc} = 0.73$, which results in a larger deviation from the experimental data. So, we may conclude that the CPW calculations are not accurate enough for this MKID's geometry. We plan to tackle this issue in the near future using other simulation tools specialized for such tasks.

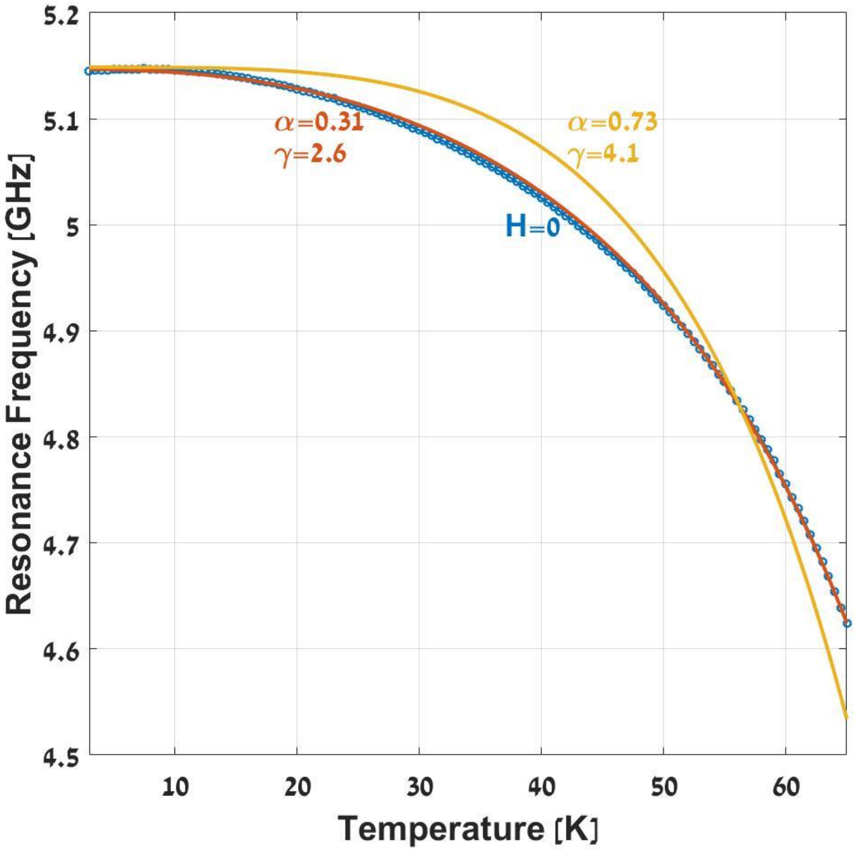

Figure 20. Resonance frequency as a function of temperature at $H = 0$. Blue points are data. Orange and yellow solid lines are fits using Eq. (44) for $\alpha_{sim} = 0.31$ and $\alpha_{calc} = 0.73$, yielding $\gamma = 2.6$ and $\gamma = 4.1$, respectively.

The temperature dependence of the resonance frequency together with the SONNET simulations allow us to find the kinetic inductance fraction. We can use the magnetic field dependence of the resonance frequency to find β_2 of Eq. (21). In general, the resonance frequency is influenced not only by vortices but also by screening currents which affect the density of the Cooper pairs and thus L_k [21,56]. As we show below, in ZFC measurements the influence of both is observed, whereas in FC measurements only the effect of vortices is observed as in these measurements the induction across the spiral stripe is uniform. Thus, the net effect of the field on f_r can be derived from FC measurements as arising from the field dependence of λ_L which appears in eq. (21). As we discussed previously, the magnetic inductance cannot be ignored. Using Eqs. (21) and (2)), this yields:

$$(44)\ f_r(H,T) \sim \frac{1}{\sqrt{\left(\lambda_L(0,T)\left(1+\beta\left[\frac{H}{H_0}\right]\right)\right)^2 * \frac{g}{dw} + L_m}} \sim \frac{1}{\sqrt{L_{k_T}\left(1+\beta\left[\frac{H}{H_0}\right]\right)^2 + L_m}}.$$

Previous calculations assumed that $T \ll T_c$ so $\lambda_{L,0} = 230\,nm$ for YBCO. The FC measurements of the MKID made at $T = 20\ K,$ so using Eq. (3) and $\gamma = 2.6$ that we found previously, we get $\lambda_{L,20K} = 235\ nm$.

The solid line in Figure 21 is a fit of Eq. (21) to the FC measurements of $f_r(H)$ at T= 20 K. Taking for YBCO, $\xi_0 = 2\,nm$ and $\Phi_0 = 2.07 \cdot 10^{-11} Gm^2$, one obtains $H_0 = 4.5 \cdot 10^3\ G,$ yielding $\beta_2 \approx 0014$ at T = 20 K for $\alpha_{sim} = 0.313$. For the analytical calculation, when $\alpha_{calc} = 0.73,$ $\beta_2 \approx 0.0092$. Converting our results from β_2 to $\beta(T) = \frac{\beta_2(T)}{H_0}\lambda_{L,0}$ [30], yields $\beta = 45.5\frac{\text{Å}}{T}$ and $\beta = 71\ \frac{\text{Å}}{T}$ for α_{sim} and α_{calc} respectively, in a reasonable agreement with the value obtained in muon spin resonance measurements where $\beta = 78\ A/T$ [30]. It worth mentioning that because we adopted the value of $\lambda_{L,0}$ from the literature, and did not measure it independently for our MKID, these results cannot help us in deciding which kinetic inductance fraction calculation method is more accurate.

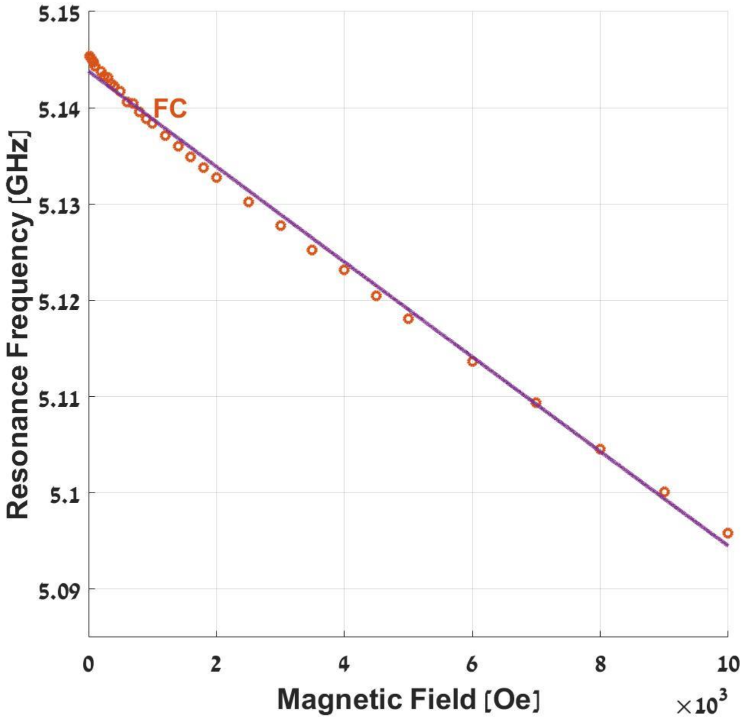

Figure 21. Resonance frequency as a function of magnetic field in FC. The solid line is a fit of Eq. (20) to the FC data.

One of the most important results of this research work, showing the difference in $f_r(H)$ between ZFC and FC measurements, was presented in Figure 19. As explained above, we ascribe the difference between the FC and ZFC data in the Figure to screening currents that are involved in ZFC but not in the FC measurements. The origin of these currents is the non-uniform induction distribution in ZFC measurements [53,54,57]. According to the Bean model for the perpendicular geometry [54,57], in the region where the field penetrates the stripe the current density is J_c and then it decreases to zero at the center of the strip. As the external field increases, the region where the critical density is J_c increases (see Figure 22). The above model assumes that J_c is uniform across the sample.

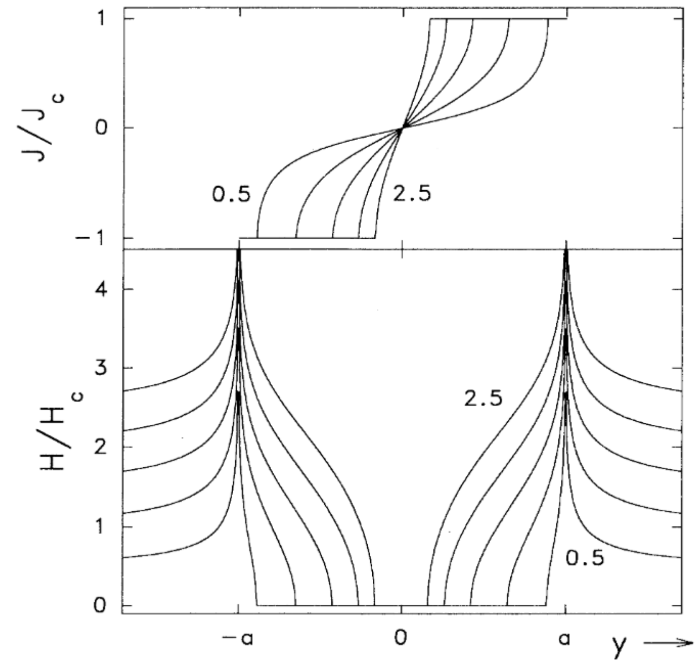

Figure 22 from Brandt *et al* [54]. Screening currents density (top) and magnetic induction (bottom) in superconducting strip of width 2a in a perpendicular magnetic field, H, which is increased from zero, as a function of the location on the strip. The depicted profiles are for H /H_c =0.5,1,1.5,2.5 . One can see that the maximum internal magnetic field achieved near the edges of the superconductors, implying that the vortices density is the highest near edges.

This assumption is no longer valid in the presence of RF current that de-pin the vortices [58]. The non-uniform distribution of the RF current density in the center strip of CPW is defined as:

$$(45)\; j_{rf}(x) = \frac{I}{S\,K\left(\frac{S}{S+2W}\right)}\begin{cases} \dfrac{1}{\sqrt{\left[1-\left(\frac{S}{S+2W}\right)^2\right]\frac{\lambda_p}{S}}}, & 0 \le \frac{S}{2} - |x| < \lambda_p \\ \dfrac{1}{\sqrt{\left[1-\left(\frac{2x}{S}\right)^2\right]\left[1-\left(\frac{2x}{S+2W}\right)^2\right]}}, & |x| \le \frac{S}{2} - \lambda_p \end{cases}$$

where I is the total current, K is complete elliptic integral from the first kind, S, W and X direction defined in Figure 3, and λ_p is pearl penetration depth as we defined previously. The non-uniform current density for our MKID geometry is present in

Figure 23 and dictates non-uniform pinning across the strip and thus a non-uniform critical current density.

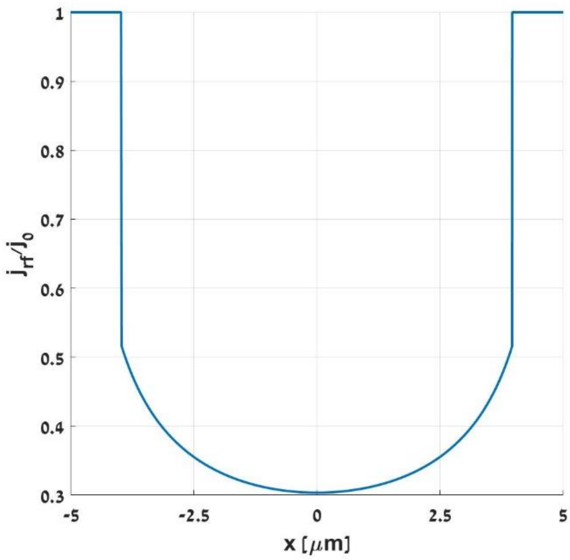

Figure 23. RF current density as a function of the location on the width of the central strip of the MKID.

The RF current density is maximum at the edges of the strip and drops sharply towards the center. As a result, the critical current density is minimum at the edges and sharply increases to a maximum value at the center of the strip. The field dependence of f_r and Q_i follow the spatial dependence of J_c; for low fields that penetrate only to the strip edges, low currents are induced and f_r and Q_i depend weakly on the field. As the field penetrates to the region where the RF current density drops sharply, high currents are induced, causing a sharp drop in f_r and Q_i. This behavior persists up to a field which we identify as the full penetration field, $H_{p,}$ where the critical current density reaches its maximum value and no further changes in the critical current occur. Above H_p, the observed changes in f_r and Q_i are due only to vortices.

The important contribution of the screening current in determining the behavior of f_r is also demonstrated in Figure 19b. These data are characterized by two regions for each temperature for which a weak field dependence is observed. These regions are close to zero field where the critical current is minimal, and at higher fields where the critical current is maximum. The difference between the two resonance values at these regions is reduced as the temperature increases, reflecting the decrease in the critical current with temperature.

The important role of the screening current is further demonstrated in FC experiments after which the field is decreased or increased. Results of such measurements are presented in Figure 24. In these measurements, a field H was applied above T_c after which the sample was cooled to 10 K. Subsequently, the field was increased or decreased. The Figure describes three such experiments for H = 100, 500, and 1000 Oe, respectively (The vertical lines in the Figure denote the fields at which the sample was cooled). Evidently, increase or decrease of the field (blue and orange points, respectively, on both sides of the vertical lines) yielded the same drop in f_r despite the significant change in the vortex density in these two processes. The same changes in f_r obtained in increasing or decreasing the external field result from the same magnitude of the screening current induced in both experiments.

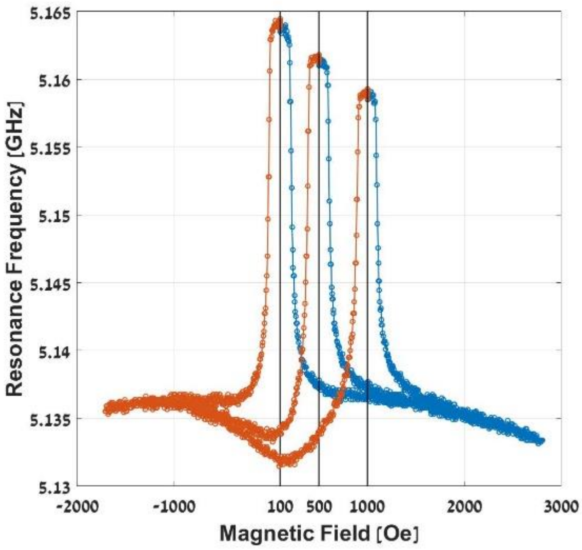

Figure 24. Magnetic field dependence of f_r after field cooling the sample from above T_c to 10 K in 100, 500 and 1000 Oe. At the target temperature, the field is either increased or decreased (blue and orange points, respectively).

8. Summary and Conclusions

I have demonstrated improved performance of thin YBCO MKID fabricated in a controlled process, yielding 2-3 orders of magnitude lower NEP and higher Q_i than previously reported. The temperature and field dependence of the resonance characteristics have been derived from the London penetration depth. In contrast to previous works who ascribed the field dependence of the resonance characteristics mainly to vortices, I show in this work the important role played by the screening currents induced by induction gradients. In FC measurements where induction gradients are absent, the resonance characteristics are controlled only by vortices, exhibiting a moderate decrease with field. In contrast, in ZFC measurements, where induction gradients exist, the effect of screening current become apparent giving rise to a more complex field dependence. Namely, exhibiting an approximately plateau region followed by a sharp decrease and subsequent moderate decrease with field. In interpreting this complex behavior, I demonstrated that the non-uniform distribution of the RF current density gives rise to a non-uniform distribution of the critical current, which dominate the behavior of the resonance characteristics in ZFC experiments at low fields.

To conclude, the work presented here is characterized by achievements in both applied and fundamental physics. Specifically, I designed and fabricated improved YBCO-based MKIDs and revealed the role of screening currents and vortices in controlling the kinetic inductance at low magnetic fields. The present work points to future challenges in fabricating HTS-based MKIDs. It also opens new fundamental questions that are outlined in the next Section.

9. Open Questions and Challenges for Future Studies

In this section I discuss a few new research topics for my future studies.

The MKID principle of operation is based on the creation of quasiparticles when a photon hits the detector. Those quasiparticles have a limited lifetime, τ_{qp}, after which they recombine to form a Cooper pair. It was shown [59] that:

$$(1)\ \tau_{qp} = \frac{\tau_0}{\pi^{0.5}}\left(\frac{k_B T_C}{2\Delta}\right)^{\frac{5}{2}}\left(\frac{T_C}{T}\right)^{\frac{1}{2}}\exp\left(\frac{\Delta}{k_B T}\right)$$

where τ_0 is characteristic electron-phonon interaction time, which is material dependent, T_c and Δ are the critical temperature and gap energy of the superconductor, respectively. The qp lifetime diverges at $T \ll T_c$, as stems from Eq. (1), is due to the decrease in thermal energy as the temperature decreases. However, previous works [60,61] on low-T_c superconductors demonstrated a saturation in τ_{qp} at $T<0.2T_c$ without explaining the phenomenon. The phenomenon indicates that at low T, there is an unknown energy source that 'feeds' the recombination process. To identify this energy source, I must understand if the saturation happens only at low T or even when $T \to 0$, because the limit defines the power of the energy source. To decide between these two options, I propose to measure τ_{qp} in LTS and HTS. In addition, it may be of interest to look for possible effects of magnetic field and transport current on τ_{qp}, because both add energy to the system which should change the saturation temperature and may help to reveal the saturation's mechanism.

My M.Sc. studies showed that the kinetic inductance (L_k) in HTS-based resonators can be affected by temperature and magnetic field. Zmuidzinas [21], indicated that DC transport currents that flow inside a resonator also affect L_k. The effect is described as: $L_k = L_k(0)(1 + \frac{I^2}{I_2^2} + \cdots)$, where I is the DC current and I_2 is expected to be of order the critical current. To the best of our knowledge, this prediction has not been tested experimentally for HTS resonators. As discussed in the thesis, the effect of the field in HTS is different than that of LTS, I therefore suggest comparing the measured $L_k(I)$ with results for LTS. In addition, these measurements are expected to yield information on $\lambda_L(I)$.

Another open issue which has emerged from my M.Sc. studies is the effect of vortices compared to screening currents on L_k. As I showed in the thesis, screening currents are dominant in the low field limit; I assumed that it is dominant up to the full penetration field, H_p. This assumption should be confirmed experimentally. Also, I assumed that the screening current distribution is changing due to the existence of RF current. However, there is a possibility for an alternative view, namely that the RF current distribution is changing due to the existence of the screening currents. I suggest experiments to distinguish between these two scenarios.

In terms of applied physics, my M.Sc. studies have pointed to several challenges, such as the need for improvement of the NEP in the YBCO-based detector. The NEP reported in this work is much better than previously reported values, but it is still well below the reported NEP for low-T_c MKIDs. In addition, a natural extension of our project should be in multiplexing several YBCO-based detectors into one device, aiming at an increase in the spatial resolution of the imaged object. Another challenge is associated with the detection of high-energy photons such as X-rays, an extension that is of interest in the security and medical industries. The challenge in detecting X-rays is because traditional MKIDs have to be made of thin films in order to increase L_k and, therefore, they do not absorb the X-ray photons.

Based on the above, I define the objectives of my Ph.D. program as follows.

9.1 Objectives

1. qp lifetime:
   a. Measuring the qp lifetime for HTS and revealing its temperature dependence at low temperatures. (In the limit $T \to 0$, I expect that in both materials τ_{qp} will diverge [59]. However, at least one experiment for LTS showed saturation of τ_{qp} below $0.2T_c$).
   b. Revealing the qp lifetime behavior at LTS and HTS as a function of magnetic field and transport current.
2. DC currents:
   a. Transport currents:
      i. Evaluating the effect of DC transport current on L_k in HTS
      ii. Explore the dependence of DC transport currents on λ_L
   b. Validating the assumption, that the screening currents are dominant (compared to the effect of vortices) is up to H_p.
3. Unveil the RF current distribution in the presence of magnetic field.

4. Applied physics:
   a. Improve the performances (NEP and Q_i) of the MKID YBCO.
   b. Design and fabricate a YBCO-based multi-component detector.
   c. Design and fabricate a detector for X-rays.

9.2 Methodology

1. qp lifetime: To evaluate the qp lifetime, I intend to use two different methods. The first one is based on photoexcitation. A photon flux hits the superconductor, creating qp that change the kinetic inductance and losses of the superconductor. Using microwave resonators, it is possible to detect the time duration of the change in the kinetic inductance which is the qp lifetime. The microwave resonator photoexcitation method works only for LTS because the high Q-factor

resonator has a typical relaxation time of $\sim 10^{-6}$ s, which is larger than the expected qp lifetime of HTS. To overcome this, I intend to build an HTS wire, which has a much lower relaxation time (~ ps) and can be used to measure qp lifetime.

The second method uses a double-tunnel junction system. On one junction a voltage $V > 2\Delta/e$ is applied, increasing the qp density, and at the same time, IV measurements are done on the other junction. (The qp lifetime can be extracted from the IV measurement using calculations in [62]). This method has been proven to be suitable for measurements of qp lifetime in LTS and HTS, contrary to the photoexcitation method, which has known limitations when measuring HTS.

2. DC currents:
    a. Transport currents: I plan to redesign the known spiral YBCO resonator so that DC currents can be applied on it. Then I plan to measure the resonator in various transport currents and magnetic fields using the MKID setup. I expect that the resonance frequency will decrease as the transport currents increase.
    b. Screening currents. The assumption can be confirmed by experimentally varying H_p which depends on the width of the fabricated wires. I plan to fabricate spiral YBCO resonators with different wire widths and examine the magnetic dependence of the resonance frequency for the different MKIDs. H_p depends also on the critical current J_c which is a material-dependent parameter. I, therefore, propose to fabricate and test also NbN-based MKIDs to examine the field dependence of the resonance frequency, identifying the range for which screening currents and vortices determine L_k.
3. RF current distribution. To distinguish between the two scenarios that were explained previously, I plan to artificially induce pinning centers at either the center of the YBCO-based resonator or near its edges. In the first scenario, as the RF current density is always low in the center of the resonator, I expect that the pinning centers in the center of the wire will affect the data only slightly. But if I consider the second scenario, where the RF current density increases in

the center as the magnetic field increases, pinning centers in the center will cause a reduction in the losses compared to resonators without pinning centers. For the pinning centers on the edge of the wire, in the first scenario, I expect a reduction in the losses, but for the second scenario, I expect a decrease in the losses at low magnetic fields, and after the magnetic field penetrates there will be a slight change in the data.

4. Improve the YBCO-based MKID performances. The geometry of the fabricated MKID was designed for detecting sub-THz photons. I suspect that the efficiency of the MKID is reduced, at least in part, in using the fabricated geometry for the detection of IR photons. I plan, therefore, to use simulation tools that will direct us in fabricating a design for IR photons. Moreover, I will also fabricate YBCO-based MKIDs with different film thicknesses. I note that thinner films increase L_k, but, on the other hand, thicker films improve absorption efficiency. To compensate for the decrease in L_k, I will narrow the wire width. All these changes in the geometry, which will be first checked by using the simulation tools, are expected to improve the MKID performance, in particular, the Q factor and the NEP.
5. Muti-component detector. A multi-component detector requires a multi-number of resonators that coupled to one transmission line; Each resonator has different resonance frequency. To do so, each resonator has a different length which yields a different resonance frequency. Moreover, in the multi-component MKID, the transmission is longer compared to single-pixel MKID, in order to contain multi-number of resonators. I intend to use simulation tools to tune each resonator, reduce its bandwidth and design a compact resonator array that each resonator in it does not affect the others.
6. MKID for high-energy photons (e.g. X-rays). As explained above, high-energy photons, such as X-rays, are not absorbed in conventional MKIDs which are made of thin films. To overcome this problem, I plan to design and fabricate a device that will be composed of two components: a thick 'absorber' that will be in thermal and electric contact with the thin resonator. The absorber is planned to have a higher critical temperature (i.e., higher energy gap), allowing quasi-particles generated in the absorber to diffuse to the resonator and to change its L_k and resonance frequency. I intend to use thin films of Nb as a resonator and thick films of NbN as an absorber, which yields

a gap energy difference. Alternatively, I intend to use NbN for both parts of the device, taking advantage of the reduction in T_c in thin films compared to the bulk.

10. References

[1] J. N. Ullom and D. A. Bennett, *Review of Superconducting Transition-Edge Sensors for x-Ray and Gamma-Ray Spectroscopy*, Supercond. Sci. Technol. **28**, 084003 (2015).

[2] I. Hakimi, N. Vardi, A. Sharoni, M. Rosenbluh, and Y. Yeshurun, *Enhancement of Photon Detection in Superconducting Nanowire Single Photon Detector Exposed to Oscillating Magnetic Field*, Appl. Phys. Lett. **118**, 232603 (2021).

[3] J. Zmuidzinas and P. L. Richards, *Superconducting Detectors and Mixers for Millimeter and Submillimeter Astrophysics*, Proc. IEEE **92**, 1597 (2004).

[4] P. K. Day, H. G. LeDuc, B. A. Mazin, A. Vayonakis, and J. Zmuidzinas, *A Broadband Superconducting Detector Suitable for Use in Large Arrays*, Nature **425**, 817 (2003).

[5] J. Baselmans, *Kinetic Inductance Detectors*, J Low Temp Phys **167**, 292 (2012).

[6] M. A. Lindeman, J. A. Bonetti, B. Bumble, P. K. Day, B. H. Eom, W. A. Holmes, and A. W. Kleinsasser, *Arrays of Membrane Isolated Yttrium-Barium-Copper-Oxide Kinetic Inductance Bolometers*, Journal of Applied Physics **115**, 234509 (2014).

[7] A. Chakrabarty, M. A. Lindeman, B. Bumble, A. W. Kleinsasser, W. A. Holmes, and D. Cunnane, *Operation of YBCO Kinetic-Inductance Bolometers for Outer Solar System Missions*, Appl. Phys. Lett. **114**, 132601 (2019).

[8] M. Naruse, T. Ando, Y. Waga, R. Kubota, S. Mima, C. Otani, T. Taino, and H. Myoren, *Superconducting Resonators with Niobium and YBa2Cu3O(7-δ) for Alpha-Particle Detectors*, J Low Temp Phys **199**, 614 (2020).

[9] K. Sato, S. Ariyoshi, S. Negishi, S. Hashimoto, H. Mikami, K. Nakajima, and S. Tanaka, *Evaluation of YBa2Cu3O(7-δ) Based Microwave Kinetic Inductance Detectors with Rewound Spiral Resonators*, J. Phys.: Conf. Ser. **1054**, 012053 (2018).

[10] J. Gao, The Physics of Superconducting Microwave Resonators, PhD Thesis, California Institute of Technology, 2008.

[11] B. A. Mazin, Microwave Kinetic Inductance Detectors, PhD Thesis, California Institute of Technology, 2004.

[12] G. Ulbricht, B. A. Mazin, P. Szypryt, A. B. Walter, C. Bockstiegel, and B. Bumble, *Highly Multiplexible Thermal Kinetic Inductance Detectors for X-Ray Imaging Spectroscopy*, Appl. Phys. Lett. **106**, 251103 (2015).

[13] A. Wandui, J. J. Bock, C. Frez, M. Hollister, L. Minutolo, H. Nguyen, B. Steinbach, A. Turner, J. Zmuidzinas, and R. O'Brient, *Thermal Kinetic Inductance Detectors for Millimeter-Wave Detection*, Journal of Applied Physics **128**, 044508 (2020).

[14] J. Luomahaara et al., *A Passive, Fully Staring THz Video Camera Based on Kinetic Inductance Bolometer Arrays*, IEEE Trans. THz Sci. Technol. **11**, 101 (2021).

[15] M. P. Oomen, AC loss in superconducting tapes and cables, PhD Thesis, University of Twente, 2000.

[16] P. W. Anderson, B. I. Halperin, and C. M. Varma, *Anomalous Low-Temperature Thermal Properties of Glasses and Spin Glasses*, Philosophical Magazine **25**, 1 (1972).

[17] W. A. Phillips, *Two-Level States in Glasses*, Rep. Prog. Phys. **50**, 1657 (1987).

[18] T. Noguchi, A. Dominjon, M. Kroug, S. Mima, and C. Otani, *Characteristics of Very High Q Nb Superconducting Resonators for Microwave Kinetic Inductance Detectors*, IEEE Trans. Appl. Supercond. **29**, 1 (2019).

[19] L. Faoro and L. B. Ioffe, *Internal Loss of Superconducting Resonators Induced by Interacting Two-Level Systems*, Phys. Rev. Lett. **109**, 157005 (2012).

[20] M. J. Lancaster, *Fundamental Considerations of Superconductors at Microwave Frequencies*, in *Microwave Superconductivity*, edited by H. Weinstock and M. Nisenoff (Springer Netherlands, Dordrecht, 2001), pp. 1–20.

[21] J. Zmuidzinas, *Superconducting Microresonators: Physics and Applications*, Annu. Rev. Condens. Matter Phys. **3**, 169 (2012).

[22] M. J. Lancaster, *Passive Microwave Device Applications Of High Temperature Superconductors* (Cambridge University Press, New York, 1997).

[23] D. Niepce, Nanowire Superinductors, PhD Thesis, Chalmers University of technology, 2018.

[24] S. K. Remillard, Two-Fluid Model Surface Impedance: A Tutorial, Tutorial, Hope Collage, 2017.

[25] A. J. Annunziata, Single-Photon Detection, Kinetic Inductance, and Non-Equilibrium Dynamics in Niobium and Niobium Nitride Superconducting Nanowires, PhD Thesis, Yale University, 2010.

[26] M. Tinkham, *Introduction to Superconductivity*, 2nd ed (McGraw Hill, New York, 1996).

[27] H. Jiang, T. Yuan, H. How, A. Widom, C. Vittoria, and A. Drehman, *Measurements of Anisotropic Characteristic Lengths in YBCO Films at Microwave Frequencies*, Journal of Applied Physics **73**, 5865 (1993).

[28] O. G. Vendik, I. B. Vendik, and D. I. Kaparkov, *Emperical Model of the Microwave Properties of High-Temperature Superconductors*, IEEE TRANSACTIONS ON MICROWAVE THEORY AND TECHNIQUES **46**, 10 (1998).

[29] S. Li-Bin, W. Yun-Fei, K. Yu-Yang, Z. Guo-Hua, L. Sheng, Z. Xue-Qiang, L. Chun-Guang, L. Hong, and H. Yu-Sheng, *A Study on the Microwave Responses of YBCO and TBCCO Thin Films by Coplanar Resonator Technique*, Chinese Phys. **16**, 3036 (2007).

[30] J. E. Sonier et al., *Magnetic Field Dependence of the London Penetration Depth in the Vortex State of YBa 2 Cu 3 O 6.95*, Phys. Rev. B **55**, 11789 (1997).

[31] A. Maeda, Y. Iino, T. Hanaguri, N. Motohira, K. Kishio, and T. Fukase, *Magnetic Field Dependence of the London Penetration Depth of Bi 2 Sr 2 Ca Cu 2 O y*, Phys. Rev. Lett. **74**, 1202 (1995).

[32] D. M. Pozar, *Microwave Engineering*, Fourth Edition (JohnWiley & Sons, Inc., 2011).

[33] N. Zobrist et al., *Design and Performance of Hafnium Optical and Near-IR Kinetic Inductance Detectors*, Appl. Phys. Lett. **115**, 213503 (2019).

[34] B. A. Mazin, B. Bumble, P. K. Day, M. E. Eckart, S. Golwala, J. Zmuidzinas, and F. A. Harrison, *Position Sensitive X-Ray Spectrophotometer Using Microwave Kinetic Inductance Detectors*, Appl. Phys. Lett. **89**, 222507 (2006).

[35] I. Colantoni et al., *Design and Fabrication of the Second-Generation KID-Based Light Detectors of CALDER*, J Low Temp Phys **193**, 726 (2018).

[36] J. Gao et al., *Strongly Quadrature-Dependent Noise in Superconducting Microresonators Measured at the Vacuum-Noise Limit*, Appl. Phys. Lett. **98**, 232508 (2011).

[37] B. A. Mazin, *Superconducting Materials for Microwave Kinetic Inductance Detectors*, ArXiv:2004.14576 [Astro-Ph, Physics:Cond-Mat] (2020).

[38] D. Bothner, T. Gaber, M. Kemmler, D. Koelle, R. Kleiner, S. Wünsch, and M. Siegel, *Magnetic Hysteresis Effects in Superconducting Coplanar Microwave Resonators*, Phys. Rev. B **86**, 014517 (2012).

[39] C. Song, T. W. Heitmann, M. P. DeFeo, K. Yu, R. McDermott, M. Neeley, J. M. Martinis, and B. L. T. Plourde, *Microwave Response of Vortices in Superconducting Thin Films of Re and Al*, Phys. Rev. B **79**, 174512 (2009).
[40] P. Lahl and R. Wordenweber, *Nonlinear Microwave Properties of HTS Thin Film Coplanar Devices*, IEEE Trans. Appl. Supercond. **13**, 2917 (2003).
[41] D. Bothner et al., *Reducing Vortex Losses in Superconducting Microwave Resonators with Microsphere Patterned Antidot Arrays*, Appl. Phys. Lett. **100**, 012601 (2012).
[42] E. Bar, D. Levi, G. Koren, A. Shaulov, and Y. Yeshurun, *Transport Properties of Ultra-Thin Granular YBa 2 Cu 3 O 7− δ Nanobridges*, Physica C: Superconductivity and Its Applications **506**, 160 (2014).
[43] *Ceraco Ceramic Coating*, https://www.ceraco.de/ybco-films/film-types/.
[44] C. P. Wen, *Coplanar Waveguide: A Surface Strip Transmission Line Suitable for Nonreciprocal Gyromagnetic Device Applications*, IEEE Trans. Microwave Theory Techn. **17**, 1087 (1969).
[45] M. Calvo, Development of Kinetic Inductance Detectors for the Study of the Cosmic Microwave Background Polarization, PhD Thesis, Sapienza Univesita DI Roma, 2008.
[46] K. Watanabe, K. Yoshida, T. Aoki, and S. Kohjiro, *Kinetic Inductance of Superconducting Coplanar Waveguides*, Jpn. J. Appl. Phys. **33**, 5708 (1994).
[47] R. N. Simons, *Coplanar Waveguide Circuits, Components, and Systems* (John Wiley & Sons, Inc., New York, USA, 2001).
[48] K. Hayashi, A. Saito, T. Sawada, Y. Ogawa, K. Nakajima, H. Yamada, S. Ariyoshi, and S. Ohshima, *Microwave Characteristics of Microwave Kinetic Inductance Detectors Using Rewound Spiral Resonators Array*, Physics Procedia **45**, 213 (2013).
[49] E. R. Brown, A. W. M. Lee, B. S. Navi, and J. E. Bjarnason, *Characterization of a Planar Self-Complementary Square-Spiral Antenna in the THz Region*, Microw. Opt. Technol. Lett. **48**, 524 (2006).
[50] *Sonnet Software*, https://www.sonnetsoftware.com/.
[51] R. E. Collin, *Foundations for Microwave Engineering*, 2. ed (A JOHN WILEY & SONS, INC.. PUBLICATION, n.d.).
[52] G. H. Rieke, *Detection of Light: From the Ultraviolet to the Submillimeter*, 2. ed (Cambridge Univ. Press, Cambridge, 2003).
[53] C. P. Bean, *Magnetization of High-Field Superconductors*, Rev. Mod. Phys. **36**, 31 (1964).
[54] E. H. Brandt and M. Indenbom, *Type-II-Superconductor Strip with Current in a Perpendicular Magnetic Field*, Phys. Rev. B **48**, 12893 (1993).
[55] J. Krupka, J. Judek, C. Jastrzębski, T. Ciuk, J. Wosik, and M. Zdrojek, *Microwave Complex Conductivity of the YBCO Thin Films as a Function of Static External Magnetic Field*, Appl. Phys. Lett. **104**, 102603 (2014).
[56] A. J. Annunziata, D. F. Santavicca, L. Frunzio, G. Catelani, M. J. Rooks, A. Frydman, and D. E. Prober, *Tunable Superconducting Nanoinductors*, Nanotechnology **21**, 445202 (2010).
[57] E. Zeldov, J. R. Clem, M. McElfresh, and M. Darwin, *Magnetization and Transport Currents in Thin Superconducting Films*, Phys. Rev. B **49**, 9802 (1994).
[58] M. Golosovsky, M. Tsindlekht, H. Chayet, and D. Davidov, *Vortex Depinning Frequency in YBa 2 Cu 3 O 7 − x Superconducting Thin Films: Anisotropy and Temperature Dependence*, Phys. Rev. B **50**, 470 (1994).
[59] S. B. Kaplan, C. C. Chi, D. N. Langenberg, J. J. Chang, S. Jafarey, and D. J. Scalapino, *Quasiparticle and Phonon Lifetimes in Superconductors*, Phys. Rev. B **14**, 4854 (1976).
[60] A. Fyhrie, P. Day, J. Glenn, H. Leduc, C. McKenney, J. Perido, and J. Zmuidzinas, *Decay Times of Optical Pulses for Aluminum CPW KIDs*, J Low Temp Phys **199**, 688 (2020).

[61] R. Barends, J. J. A. Baselmans, S. J. C. Yates, J. R. Gao, J. N. Hovenier, and T. M. Klapwijk, *Quasiparticle Relaxation in Optically Excited High- Q Superconducting Resonators*, Phys. Rev. Lett. **100**, 257002 (2008).
[62] J. L. Levine and S. Y. Hsieh, *Recombination Time of Quasiparticles in Superconducting Aluminum*, Phys. Rev. Lett. **20**, 994 (1968).